TECHNICAL ARTICLE

Tension–Compression Flow Asymmetry as a Function of Alloy Composition in the Al-Si System

K. Singh and B.P. Kashyap

Al-Si alloys of hypoeutectic, near-eutectic, and hypereutectic compositions, prepared from commercial pure aluminum and silicon, were investigated to study their tensile and compressive properties. The microstructures in as-cast stage were found to be refined after subsequent remelting and casting for two, five, and ten cycles. The proportion of eutectic phase and silicon particles increased with silicon content and influenced the nature of stress–strain curves. Both tensile and compressive stress–strain curves exhibited increase in flow stress with increasing strain, which could be expressed by Hollomon type relationships, but the tensile deformation occurs at lower flow stress than that in compression. While tensile specimens showed limited elongation to failure, the compression ones exhibited larger strains, up to 30% without failure. The tension–compression flow asymmetry was noted to vary as a function of the number of remelting cycles and of the silicon content in the alloy. The work hardening rate showed only stage III behavior in tension but both stage III and IV behavior in compression. The flow stress, including the yield strength, in compression was found to increase with decrease in grain size. However, in tensile deformation, instead of grain size effect, the yield strength was noted to increase with the decrease in inter-particle spacing. In both these cases, the Hall–Petch type relationships were found to be obeyed.

1. Introduction

With the increasing demand for lightweight materials in the field of automotive, space, construction, electronic packaging, etc., the as-cast aluminum-silicon (Al-Si) alloys have become materials of revived interest. Predominantly, these alloys possess excellent properties like good castability, high specific strength, high thermal conductivity, low coefficient of thermal expansion, and high corrosion resistance (Ref 1-4). These properties get substantially influenced through compositional and melting–casting practice. Based on the Si content, the binary Al-Si alloys are compositionally divided into three categories hypoeutectic (< 12.6 wt.% Si), hypereutectic (> 12.6 wt.% Si), and eutectic (∼ 12.6 wt.% Si). As the silicon content increases, the inhomogeneity in the size, shape, and distribution of the primary silicon in the aluminum matrix also increases, which, in turn, substantially influences the physicomechanical properties of Al-Si alloys (Ref 5, 6).

It is known (Ref 5, 7-11) that as the strength increases, the ductility decreases with increasing silicon in Al-Si alloys. In some materials, like Mg (Ref 12-17), Ti (Ref 18-20), Ni (Ref 21-23), Cu (Ref 24-27), and Al (Ref 28-31) -based alloys, the material response differs between the uniaxial tension and

compression tests. Generally, the yield strength in compression was found to be more than that in the tension. The difference between the compressive yield strength and tensile yield strength is termed as the yield asymmetry, which can be affected by microstructural and deformation parameters (Ref 19) as elaborated in the next paragraph.

Chang and Chi (Ref 32) investigated the effect of texture and strain rate on the Tension–Compression Asymmetry (TCA) in AZ31 magnesium alloy. The TCA decreased with an increase in strain rate and texture anisotropy. The TCA in magnesium and magnesium alloys occurs because an asymmetric twinning mechanism dominates the deformation of the hexagonal closed pack (HCP) structure. In a similar study, Lin et al. (Ref 14) also showed the TCA in AZ31 magnesium alloy deformed under uniaxial tension and compression tests which can be affected by texture and polar nature of twining, extension and contraction twining. Polarity means asymmetry and non-polarity means symmetry which, in the case of plastic deformation by twinning, implies to the differing nature of crystallographic response of hcp crystal like Mg and its alloys. There exist extension and contraction twins with their characteristic crystallographic response to deformation. Initially, the extension twin occurs parallel to c-axis in tensile loading and perpendicular to c-axis in compressive loading. Later, extension twin, with lower critical resolved shear stress, is dominant in compression to result in lower yield strength than that in tension; the higher yield strength in tensile deformation is ascribed to the almost complete suppression of extension twins. Compressive deformation is further facilitated by transformation of extension twins into contraction twins by crystallographic reorientation to the untwinned matrix. In some more studies (Ref 17-19), the effects of grain size/bimodal structure (dual fine grain and coarse grain structure) and precipitate shape contributed to asymmetric flow property. The bimodal grain

K. Singh and **B.P. Kashyap**, Department of Metallurgical and Materials Engineering, Indian Institute of Technology Jodhpur, Karwar, Rajasthan 342030, India. Contact e-mail: bpk@iitj.ac.in.

structure caused a lower TCA as compared to the uniform grain structure. The precipitates, while remaining inside the existing twins, do not get sheared but produce unrelaxed back-stress and prevent the growth of twins; thereby, the precipitates reduce the tendency of yield asymmetry caused by twinning in magnesium alloys (Ref 17).

Neeraj et al. (Ref 20) observed TCA in two-phase α/β Ti-alloy, Ti-6Al-2Sn-4Zr-2Mo, and Ti-6Al titanium alloy during the room temperature creep test. They explained the sources of asymmetry to be (i) the activation of $<c + a>$ dislocation slip, (ii) asymmetry in the CRSS (critical resolved shear stress) values between tension and compression, and (iii) $<a>$ type screw dislocation mobility. Syed et al. (Ref 18) performed uniaxial tension and compression tests on a two-phase Ti-5Al-3Mo-1.5 V titanium alloy and found the effect of microstructural variation on TCA. Zhang et al. reported (Ref 33) the asymmetric behavior of properties in Ti-6.5Al-2Zr-1Mo-1 V titanium alloy from their high-temperature tests. The yield strength in tension was found to be more than that in compression, and the asymmetry decreased as the temperature increased.

Tsuno (Ref 22) investigated the effect of temperature on tension–compression yield asymmetry during the creep test for Ni-based superalloys and reported the TCA to decrease with increasing test temperature. TCA was also found in nanocrystalline copper and Cu-based alloys (Ref 24, 34), Fe-10Cu alloy, and Al-10Ti-2Cu alloy.

Sahoo and Smith (Ref 35) investigated the tensile and compressive properties of eutectic Al-Si alloy as a function of directional solidification growth conditions. This led to greater compressive strengths than that in tension under all growth conditions. Similarly, Vnuk et al. (Ref 36) studied the variation in hardness as a function of the solidification growth condition and reported the hardness as a maximum in the chill cast condition. Hong (Ref 31) analyzed the TCA of hardening in Al matrix composite material and ascribed the TCA to the difference in fracture mechanisms between tension and compression loading. In the tension test, the crack initiates perpendicular to the loading direction, and the void coalescence leading to fracture is facilitated easily in the material. In the case of compression, the crack starts parallel to the loading direction, and the voids get suppressed, delaying the occurrence of fracture. An investigation was carried out by Meininger et al. (Ref 37) by using cyclic deformation of aluminum alloy 7075 in the T6 and T651 temper conditions to observe the TCA. At low plastic strain amplitude, the maximum cyclic strength in compression was reported to be greater than that in tension for T6 temper condition, whereas, for T651 temper condition, the reverse was true. However, this trend was reported to change with further deformation due to difference in cyclic hardening behavior. The TCA was explained to arise from the introduction of strain localization seen in the form of quench band and precipitate cutting mechanism during deformation. Tucker et al. (Ref 30) analyzed the strain rate effect on plasticity, damage, and fracture mechanism of three aluminum alloys. They observed the asymmetric behavior in tension, compression, and torsion properties. In another study, Li (Ref 38) observed orientation-dependent tension–compression asymmetric nature in Al-Fe alloys. A considerable effect of deformation temperature was also indicated on the TCA of an extruded nanocrystalline Al-Fe-Cr-Ti alloy and A356-T7 aluminum alloys (Ref 39, 40). In an exciting study, Wang et al. (Ref 41) published an article on the deformation behavior of amorphous silicon under tension and compression tests. It was reported that the yield strength in tension was more than that in compression.

There are many factors that can affect the tension–compression behavior and cause asymmetry in the properties of metals and alloys. These factors include

(i) Process condition, (ii) Compositional variation, (iii) Heat treatment condition, (iv) Deformation condition (strain rate, temperature, etc.); (v) Microstructural parameters (grain size, phase fraction, etc.). However, most of the literature cited above on TCA is based on the effects of heat treatment conditions and the deformation condition, with only limited data being available on the effects of process conditions and compositional variation.

The tensile and compressive properties of materials are essential for a range of industries. Al-Si alloys of hypoeutectic (Al-6 to 8Si) (Ref 42), eutectic (Al-11 to 13Si) (Ref 43) and hypereutectic (Al-20Si) (Ref 44) compositions with their variants (or impurities) are widely used in automotive and aerospace industries (Ref 45). For example, Al-6.5 to Al-7.5 Si alloys are used for cylinder block, cylinder head, speed transmission housing, and wheel rim in automotive (Ref 45); rear frame avionics brackets, tail rotor gearbox, and over-wing emergency door exit in the aeroplane. The eutectic Al-Si alloy is used as an automotive piston material (Ref 43), whereas hypereutectic Al-Si is also recommended for use as a cylinder liner (Ref 44). Higher Si-containing Al-Si alloys, up to 70 wt.% Si, are also becoming promising for electronic packaging (Ref 46, 47). Most of these components are used in the as-cast stage, and they vary in size and shape; when used in service, they might encounter different tensile and compressive stresses, with the asymmetry in mechanical properties. Therefore, it is important to know the tensile and compressive properties of Al-Si alloys prepared by melting and casting by employing the commercial base elements aluminum and silicon, containing the common impurities present in them. In this study, tensile and compressive properties of exemplary hypoeutectic, near-eutectic, and hypereutectic Al-Si alloys, in as-cast conditions along with a number of remelting cycles, were investigated to examine the nature of variation in microstructure and its relation with deformation behavior.

2. Materials and Methods

Al-Si binary alloys, which have a range of compositions from hypoeutectic (Al-5%Si) to hypereutectic (Al-40%Si), including the near-eutectic (Al-15%Si), were made by melting commercial pure aluminum (99.95%) and silicon (99.5%) in a high-frequency induction furnace. Melting was carried out in a graphite crucible at 750 ± 5 °C for hypoeutectic and near-eutectic compositions, whereas the hypereutectic alloy was melted at a set temperature of 900 ± 5 °C. The molten form of the Al and Si in the crucible was stirred intermittently and held for 15-20 min to attain the homogeneous liquid mixture condition. Finally, the melt was poured into a conical-shaped metal mold to get an ingot of 100 mm in length, 20 mm in diameter on the bottom side, and 25 mm in diameter on the upper side.

The cast ingots were cut into small pieces for remelting. The same were put again into the graphite crucible at the respective temperatures for the chosen compositions, as mentioned in the above text. The remelting process was planned for two

remelting cycles, five remelting cycles, and ten remelting cycles. Remelting cycle here means the repetition of melting and casting of the first cast ingot. For example, two remelting cycle implies that after first regular melting and casting, the ingot was cut into pieces and remelted and cast twice to get the two cycles of remelted ingot.

The alloys used in the present work, Table 1, have the same range of compositions as used in our previous work (see Table 1 of Ref 48). This table is reproduced with some re-designation (columns 1 and 2) as Table 1 here for the sake of convenience. Instead of writing individual compositions every time, it was chosen to use the generic compositions to represent the hypoeutectic, near-eutectic, and hypereutectic alloys throughout. Given in Table 1 are the detailed compositions with re-designations of the alloy compositions as Al-5Si, Al-15Si, and Al-40Si within the composition variations seen for each alloy category as a function of remelting cycle. The slight variation in alloy composition (including wt.% Si) within the hypoeutectic, near-eutectic, and hypereutectic alloys appears to be caused by the impurities present in commercial aluminum and silicon used for making the alloys, and the effects of remelting and inherent experimental limitations. In Table 1, CS represents the first melt and cast condition, whereas upon remelting and casting, these alloys are designated by RM with the cycle number given as prefix for each category of alloy composition and remelting cycle.

After melting and casting, all the ingots were machined on a lathe to get a cylindrical rod of 10 mm diameter. The samples for metallography, tension test, and compression test were cut from the as-cast ingots and given standard cylindrical shape of the dimensions listed in Table 2 by using the lathe machine.

Metallographic samples were prepared by using the standard mechanical polishing method which consisted of first using emery papers of different (180 to 2000) grits and then the cloth polishing with colloidal silica slurry of 0.5 μm size on a rotating wheel at the final stage. The microstructural examination was performed on both an optical microscope (Leica DM750) and a scanning electron microscope (Zeiss LEO). The tension and compression tests at an initial strain rate of 10^{-4} s^{-1} were conducted on an EZ50 universal testing machine of 50 kN capacity at room temperature. The compression test was terminated at the strain level of -0.40 for hypoeutectic and near-eutectic Al-Si alloys, but for the hypereutectic alloy, it was limited by the fracture occurring approximately between strains

of -0.23 to -0.28. After the tensile tests, the fracture surfaces of the tensile specimens were examined by using the scanning electron microscope (SEM).

3. Results

3.1 Microstructure

Typical scanning electron micrographs taken to represent the effects of composition (horizontally along the rows) and remelting cycle (vertically along the column) are shown in Fig. 1, whereas optical microscopy was used for the measurements of grain size and volume fraction of α-Al matrix and Si phases. The results on the same samples were presented elsewhere (Ref 48). In the hypoeutectic and near-eutectic alloys, the major phase present is α-Al which acts as a matrix phase. The other is a eutectic mixture of Al and Si, (Al + Si). With adding more silicon, beyond the eutectic composition in the alloys, the Si particles precipitate as pure silicon and form a new phase, viz. primary silicon phase. The primary Si can be precipitated in a blocky or plate-like structure depending on the wt.% Si and also seen is the growth of the silicon particles (Ref 49). The arrows in the micrographs indicate the phases present to distinguish them from each other.
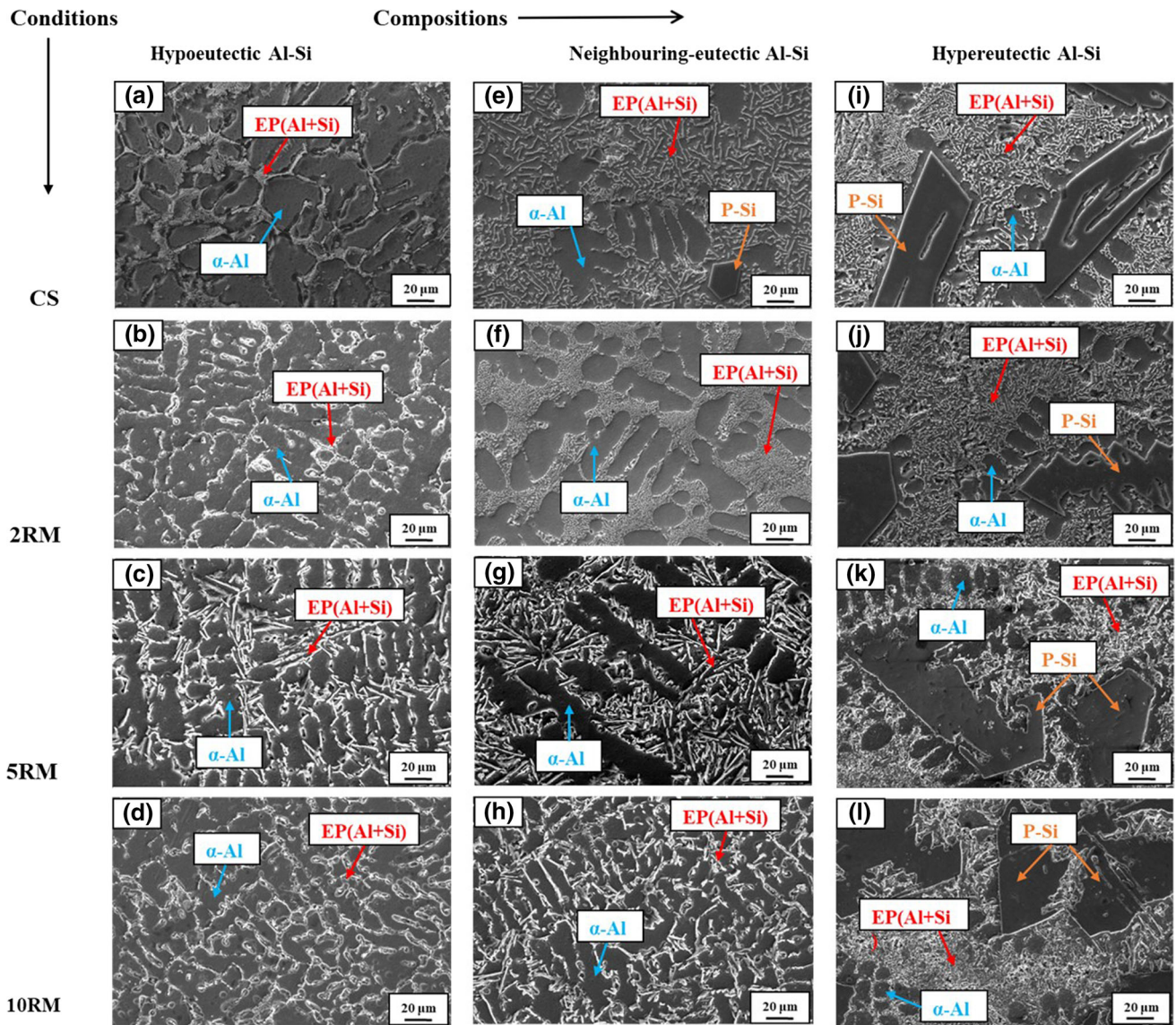
3.2 Mechanical properties

3.2.1 Stress–strain curves. Figure 2(a),(b), and (c) and Fig. 2(d),(e), and (f) illustrates the engineering stress–engineering strain curves of Al-Si alloys of different compositions and remelting cycles obtained from tension and compression tests at room temperature, respectively. The yield strengths (YS) obtained from tension and compression tests are listed in Table 3. Also included in this table are the tensile elongations

Table 2 Sample dimensions for different test purposes

Test	Sample dimension
Metallography	Dia. = 12 mm, height = 4 mm
Tension	Gage dia. = 5 mm, Gage length = 20 mm
Compression	Dia. = 8 mm, Height = 12 mm

Table 1 Classification of Al-Si alloys with their nominal compositions (wt.%) and variants their of (column 3-6) along with designation (columns 1and 2)

| Nominal composition	Melting and casting condition	Si	Fe	Mg	Al
Hypoeutectic Al-Si Alloy (Al-5Si)	CS	6.9	0.34		Balance
	2RM	5.43	0.33		Balance
	5RM	4.85	0.36		Balance
	10RM	5.02	0.77		Balance
Near-eutectic Al-Si Alloy (Al-15Si)	CS	17.12	0.48		Balance
	2RM	15.28	0.46	0.41	Balance
	5RM	17.68	0.52		Balance
	10RM	15.24	0.59		Balance
Hypereutectic Al-Si Alloy (Al-40Si)	CS	42.69	0.85		Balance
	2RM	40.29	0.68		Balance
	5RM	39.88	0.68		Balance
	10RM	39.68	0.76		Balance

Fig. 1 SEM micrographs for different compositions and remelting cycles (RM) of Al-Si alloys, showing increasing primary Si and eutectic phases with increasing Si content and refinement in microstructure with increasing remelting cycle (Here, CS = cast sample, RM = Remelting sample with their cycle numbers given by prefix, P-Si stands for primary Si)

and ultimate tensile strengths. For the hypereutectic Al-Si alloy, the stress–strain curves from tensile tests (Fig. 2c) show only elastic deformation with an almost negligible plastic regime, irrespective of the number of remelting cycles. Therefore, for the sake of comparison of tensile properties with that of other hypoeutectic and near-eutectic compositions of Al-Si alloys, the yield strength, ultimate tensile strength, and fracture strength all are taken to be the same in the case of hypereutectic alloy. As shown in Fig. 2(d),(e), and (f), the stress–strain curves obtained from compression tests were plotted as a function of Si content and the number of remelting cycles. The plots were limited to 30% strain level for hypoeutectic and near-eutectic Al-Si alloys because the stress started to increase rapidly as a function of strain, Fig. 2(d), and (e), approaching the stage of friction effect on deformation. Thus, the tests in these cases were terminated before fracture. In the case of hypereutectic Al-Si alloy, the compression samples diagonally cracked down in

the loading direction at much lower strain values ($\sim$ 23 to 28%), closer to fracture level but still not split into two fracture pieces.

For the sake of comparing the flow stress between tension and compression tests, the values of engineering stresses were taken at comparable strain levels from both the tension and compression stress–strain curves. In Fig. 3(a), and (b), the typical stress–strain curves were taken to observe the nature of flow stress in tension and compression for as-cast and after ten remelting cycles.

Further, it can be seen that the tensile yield strength (TYS) and ultimate tensile strength (UTS) increase with increasing Si content of Al-Si alloys from hypoeutectic composition to near-eutectic composition. The maximum TYS of 119 MPa and maximum UTS of 181 MPa are obtained for near-eutectic alloy composition. With further increase in Si content to hypereutectic composition, surprisingly, the TYS and UTS are noted to decrease in spite of more Si present in the alloy. This variation
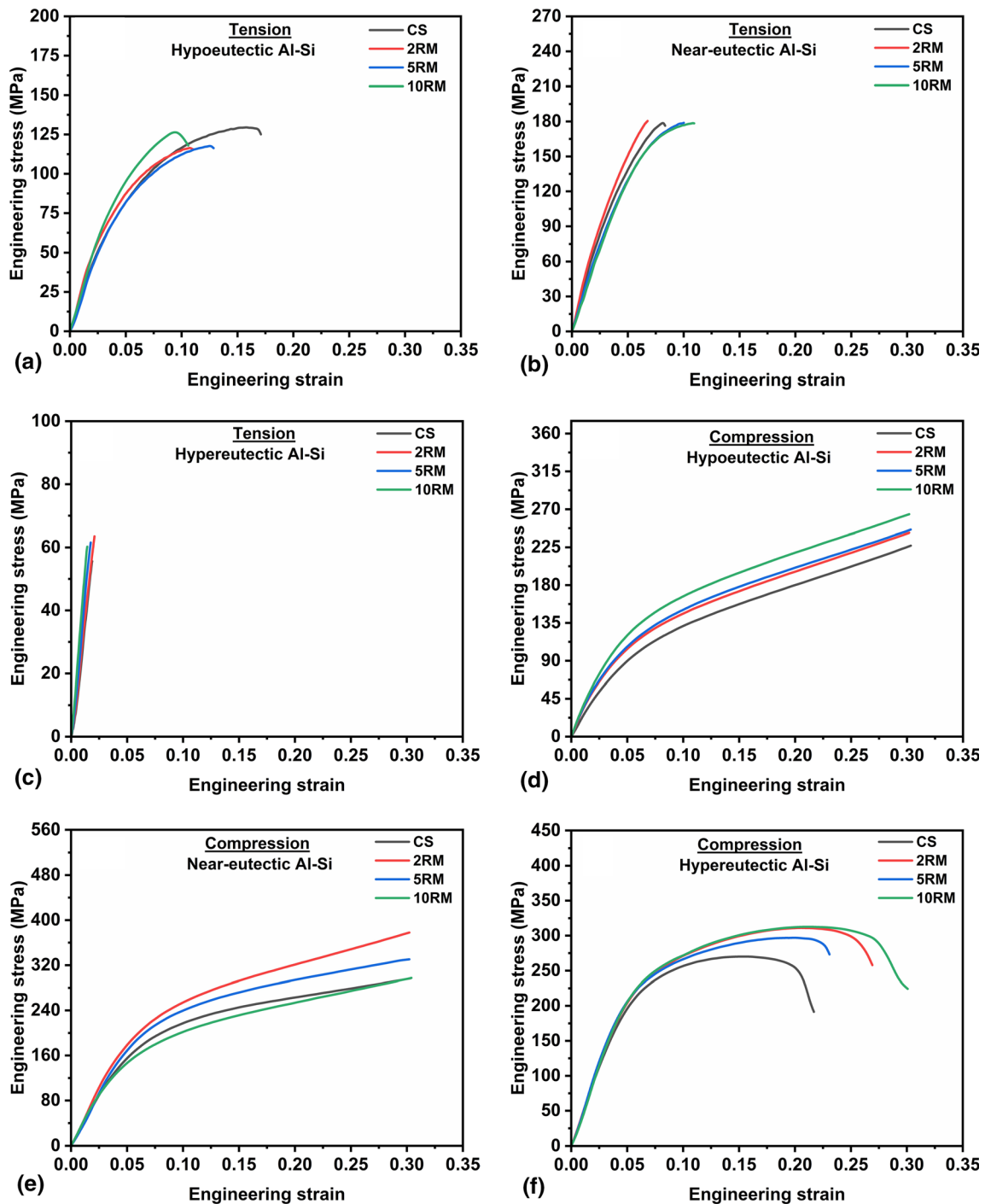
Fig. 2 Stress–strain plots obtained from tension (a,b,c) and compression tests (d,e,f) for different Al-Si alloy compositions and remelting cycles; each with as-cast, 2 remelting, 5 remelting, and 10 remelting cycles (Here, CS = cast sample, RM = Remelting sample with their cycle numbers given by prefix.)

in TYS and UTS with increasing Si content is shown in Fig. 4(a). However, the ductility plotted as a function of Si content shows an exponential fitting of a continuously decreasing trend with increasing Si, Fig. 4(a). Similarly, the uniform strain value is noted to decrease with increasing Si content, as listed in Table 3. The TYS, UTS, and elongation values are plotted as a function of the number of remelting cycles, Fig. 4(b). No effect of remelting cycle on TYS and UTS was found except that there appears to be an increase in TYS with

an increasing number of remelting cycles only in near-eutectic composition. Both % uniform strain and % elongation are noted to change in an irregular manner with increasing remelting cycles. Still, overall, the value of uniform strain and elongation was found to decrease after ten remelting cycles compared to the single melting and casting condition.

From Fig. 5(a), it can be observed that the compressive yield strength (CYS) increases with increasing Si content. However, the increase in CYS as a function of Si content

Table 3 Tensile and compressive properties of Al-Si alloys of different compositions upon various remelting cycles

Alloy composition	Number of Remelting cycle	Tensile Properties				Compression Properties		
		Yield strength, MPa	Ultimate tensile strength, MPa	Uniform strain, %	Plastic elongation, %	Yield strength, MPa	Ultimate strength* (Proof stress at 10% strain), MPa	Fracture strain (Plastic), %
Hypoeutectic Al-Si alloy	0	59	130	12.8	14	84	176	…
	2	53	117	8.5	10	92	185	…
	5	59	118	9.4	11.7	104	191	…
	10	66	129	6.7	7.7	111	212	…
Near-Eutectic Al-Si alloy	0	89	179	5.5	5.6	166	256	…
	2	87	181	4.4	4.4	189	306	…
	5	111	178	3.2	3.2	177	287	…
	10	119	179	6.3	6.4	150	241	…
Hypereutectic Al-Si alloy	0	53	53	…	…	184	270, 270	19.2
	2	55	55	…	…	201	305, 311	22
	5	54	54	…	…	205	293, 297	18.7
	10	54	54	…	…	194	307, 313	24.5

*Two values of ultimate compressive strength are given in those cases where the samples failed just after reaching above 10% proof strain
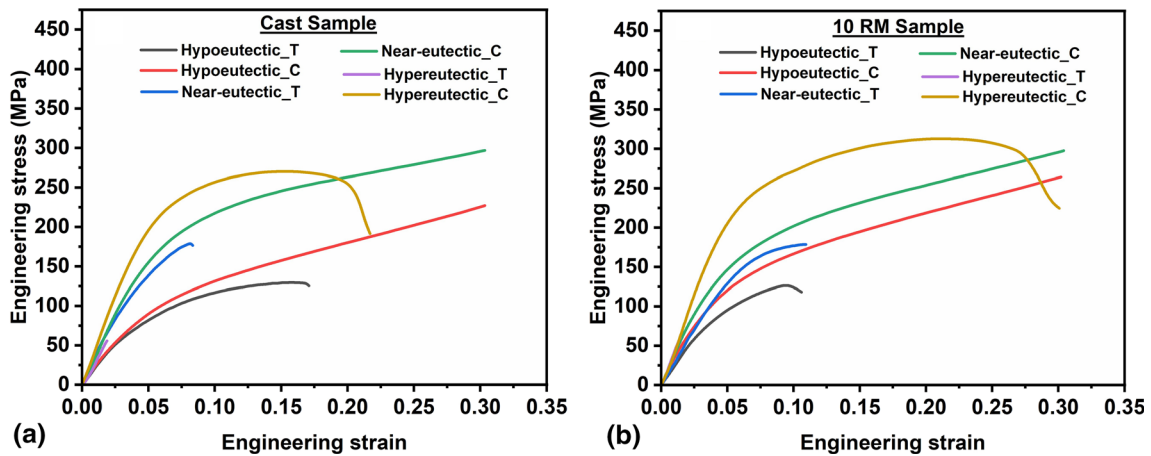

Fig. 3 Typical stress–strain curves replotted to compare the tensile (T) and compressive (C) flow behavior for (a) as-cast and (b) 10 times remelting conditions
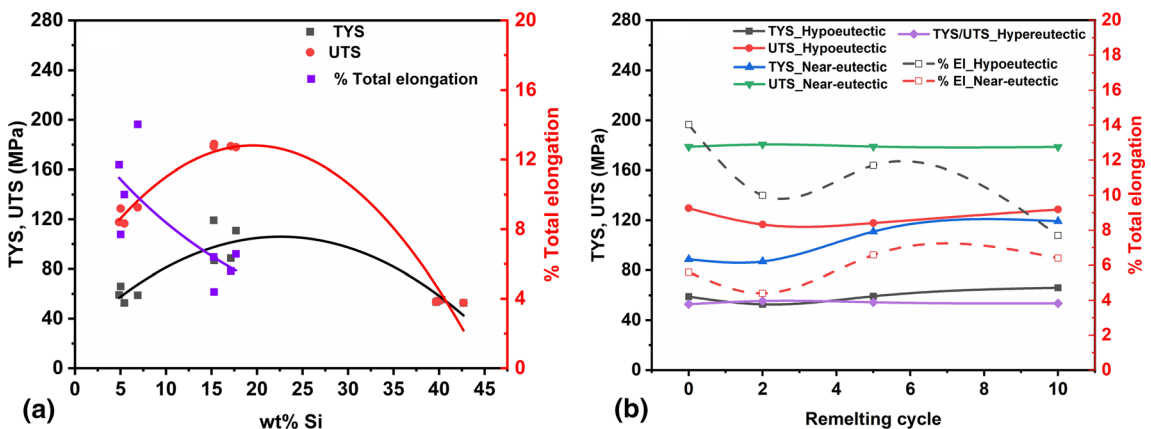
Fig. 4 Variation in tensile yield strength (TYS), ultimate tensile strength (UTS), and % total elongation as a function of (a) Si content, and (b) number of remelting cycles

between the hypoeutectic alloy and near-eutectic alloy is more sensitive than that between near-eutectic and hypereutectic alloys, which rather tends to suggest saturation in CYS. The maximum value of CYS is noted to be 205 MPa in the hypereutectic Al-Si alloy, Table 3. A fixed value of strain (at 10% strain level for hypoeutectic and near-eutectic Al-Si
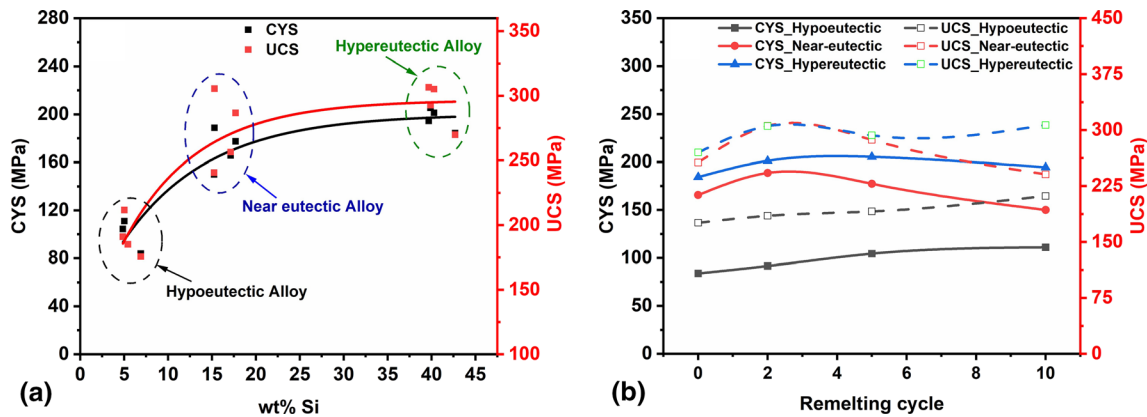
Fig. 5 (a) Variation in compressive yield strength (CYS) and that considered as ultimate compressive strength (UCS) to reflect the flow stress for the purpose of comparison (proof stress at 10% strain) with the yield strength as a function of Si content, and (b) Variation in compressive yield strength (CYS) and considered ultimate compressive strength (UCS) as a function of the number of remelting cycles. The data encircled for hypoeutectic, near-eutectic and hypereutectic alloys are taken from Table 1 for Si content and Table 3 for CYS and UCS

alloys) was selected to get the compressive flow stress (treated as equivalent ultimate compressive strength (UCS)) values to make a comparison of this property among all the samples of different compositions and remelting cycles. This strain value was taken near to the maximum % elongation in tension (14%) and is also near to the minimum value of strain that was obtained in compression tests (18.7%). An examination of the variation in ultimate compressive strength (UCS) as a function of Si content revealed it to increase and reach saturation with an increase in Si content of Al-Si alloys, as shown in Fig. 5(a); a maximum value of UCS was obtained to be 307 MPa in the hypereutectic alloy, listed in Table 3.

Figure 5(b) shows the plot of compressive yield strength and the considered ultimate compressive strength as a function of remelting cycle for all the three compositions of Al-Si alloys investigated. The values of CYS and UCS were found to increase continuously with an increase in remelting cycle in hypoeutectic Al-Si alloys. However, in near-eutectic and hypereutectic Al-Si alloys, the CYS and UCS values show an irregular trend, mostly, first, an increase and then decrease as a function of remelting cycle, as shown in Fig. 5(b).

3.2.2 Work Hardening Behavior. Work hardening rate (θ) can be determined by differentiating the flow stress (σ) with respect to strain (ε) from the plastic region of the stress–strain plots, viz. ($\theta = d\sigma/d\varepsilon$). The typical work hardening plots (θ versus ε) for different compositions and for as-cast as well as for ten remelting cycles of Al-Si alloys are presented in Fig. 6(a), and (b), from the tension and compression tests. The work hardening rate is noted to decrease with increasing strain in all the cases, but in compression, it attains constant or saturation values toward larger strains (stress). The maximum work hardening rate is found in the hypereutectic Al-Si alloys in compression, whereas the hypoeutectic alloy exhibits the minimum work hardening rate in both tension and compression tests. It is also noted that the work hardening rate increases with increasing Si content. A significant variation in peak work hardening rate was observed with the number of remelting cycles (not shown here) but in an irregular manner.

The plastic region of the stress (σ)–strain (ε) curves, obtained from tensile and compressive tests, was also analyzed by using the Hollomon relationship (Ref 50).

$$\sigma = K\varepsilon^n \qquad\qquad (Eq\ 1)$$

where K is the strength coefficient and n is the strain hardening exponent. The Hollomon-type plots were made for all tensile and compressive flow curves. Typical Hollomon type plots are presented in Fig. 7(a) to bring out the effects of (i) composition (hypoeutectic and near-eutectic), (ii) remelting cycle, and (iii) tensile *versus* compressive flow, as marked and given in the legend of the figure. The Hollomon plot reveals three regions in Fig. 7(a), and the values of K and n so obtained in different regions along with the transition stages are listed in Table 4. Different regions were identified by extrapolating the linear trend lines of two adjacent regions in Fig. 7(a) and taking their intersection points as a transition point between the two regions. These transitions are given by the symbol ε (strain) with appropriate suffixes in Table 4. The range of strains can be obtained from the difference between two such adjacent ε values. The magnitudes of K and n are found to increase with increasing Si content, and they are also higher in compression than that in tension. No such distinct effect of the remelting cycle is noted here.

Also, an attempt was made to explore if there exists any relationship between the Hollomon parameters K and n themselves. For this purpose, the mean values of these parameters over different regions were considered, and the same are plotted separately for compressive (K_c versus n_c for hypereutectic alloy) and tensile (K_t versus n_t for hypoeutectic and near-eutectic alloys) flow in Fig. 7(b). Interestingly, K and n are found to have linear relationships of type:

$$K = An \pm B \qquad\qquad (Eq\ 2)$$

where A and B are constants, whose magnitudes and the correlation coefficients are listed as an inset in Fig. 7(b) for the materials in which this relationship was followed clearly. However, no clear trend between K and n was obvious from the compressive stress–strain curves of hypoeutectic and near-eutectic compositions. The linear fit of the data for hypoeutectic and near-eutectic compositions in compression (not shown here) led the R^2 values to be far below (0.06 and 0.3, respectively) the acceptance level for linearity. Thus, no relationship between K and n could be obtained for these cases in compression and so also for hypereutectic Al-Si alloy in tension, where no plastic deformation occurred.
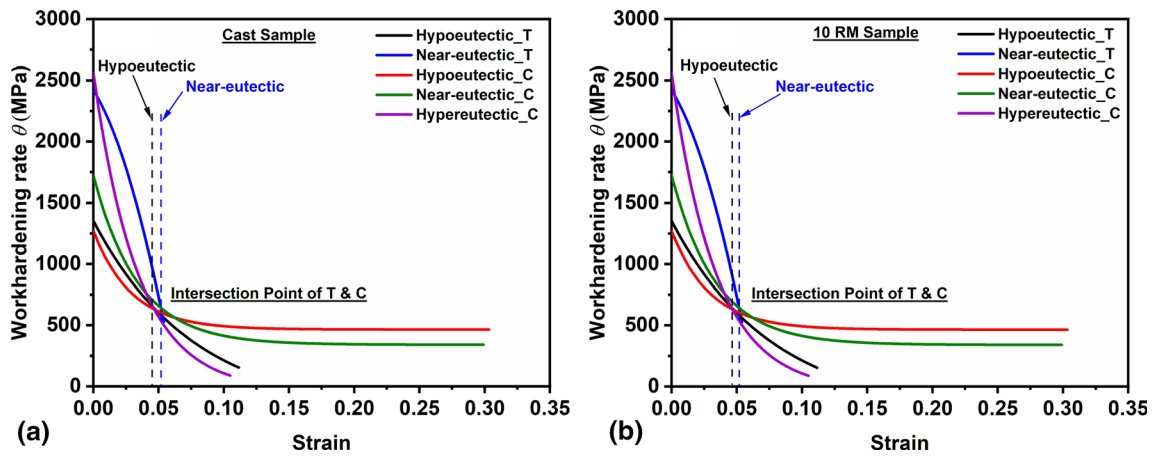
Fig. 6 Work hardening rate of Al-Si alloys as a function of strain in tension (T) and compression (C) for (a) as-cast samples, and (b) for 10 times remelting samples
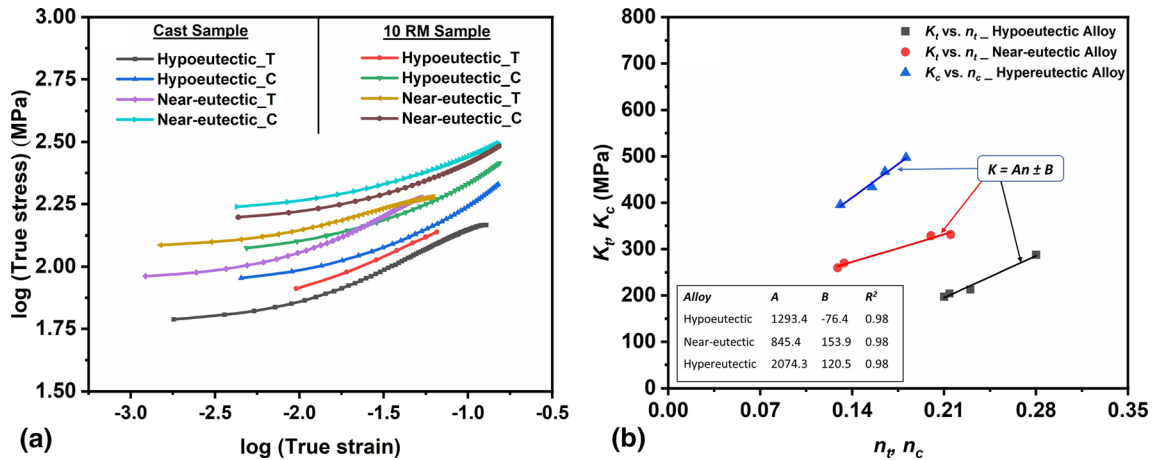

Fig. 7 Typical Hollomon plot from the tensile and compressive stress–strain curves of hypoeutectic and near-eutectic Al-Si alloys for as-cast and ten remelting cycles (a), and (b) plots of mean value of the Hollomon parameters for compressive (K_c vs. n_c) and tensile (K_t vs. n_t) tests

3.2.3 Asymmetry in Tension/Compression Properties. Here, the term asymmetry represents the nature of deformation of the material, which is different in uniaxial tensile and compressive loading. The difference between yield strength in compression (CYS) and that in tension (TYS) is defined as yield strength asymmetry (YSA = CYS-TYS). Unlike the yield strength asymmetry, not much is presented in the literature about the asymmetry in other properties of stress–strain curves. Here, an attempt is made to examine the nature of tensile and compressive stress–strain curves closely to bring out the possible differences between the two types of loading curves. While there occurs ultimate tensile strength, no such ultimate strength in compression is common except for either the fracture strength or the stress where the friction starts dominating, and the apparent flow stress starts increasing rapidly. In view of this, considered here are (i) the difference in flow stress between tensile and compressive stress–strain curves through proof stresses at selected common strain levels, although limited by the much smaller elongations in tension as compared to the maximum attained strains in compression; (ii) comparison of flow stress with the stresses in compression that correspond to the same plastic strains at which the UTS were

noted in tensile tests; (iii) comparison of parameters (Table 4) related to the nature of stress–strain curves like stages of work hardening and Hollomon relationship.

Figure 8(a) shows the plot of asymmetric behavior at the yield point for different Si content as a function of the number of remelting cycles. The asymmetry in yield strengths was found to increase with increasing Si content in Al-Si alloys, with the maximum value of 151 MPa for the hypereutectic Al-Si alloy. The YSA is observed to increase up to five remelting cycles, but then it decreases for tenth remelting cycles for hypoeutectic and hypereutectic alloys, whereas for near-eutectic Al-Si alloy, the YSA increases up to two remelting cycles (102 MPa), and thereafter, it decreases continuously with the increasing number of remelting cycles. Figure 8(b) illustrates the variation in flow stress asymmetry ($\sigma_{fA} = \sigma_c - \sigma_t$) as a function of strain for hypoeutectic Al-Si composition, whereas Fig. 8(c) illustrates the same for the near-eutectic composition. It may be pointed out here that, in spite of the variation in engineering strain from ~ 0.096 for 10RM to 0.15 for CS, Fig. 2(a), the proof stress by linear offset method could be obtained only up to 0.04 engineering strain for comparative study of flow stress asymmetry ($\sigma_{fA} = \sigma_c - \sigma_t$) plot as a function of strain from all the stress–strain curves. An attempt was made

Table 4 Values of Hollomon parameters—strength coefficient (*K*) and strain hardening exponent (*n*), calculated as a function of remelting cycle and alloy composition, suggesting three different regions from the log(σ)-log(ε) plots in tension and compression tests

K (MPa), *n*, ε		Remelting conditions			
		CS	2RM	5RM	10RM
Hypoeutectic Al-Si alloy					
Tension					
Region I	K_{tI}	106.267	96.984	111.429	287.806
	n_{tI}	0.088	0.087	0.095	0.275
	ε_{tI}	0.009	0.007	0.01	…
Region II	K_{tII}	222.792	271.644	225.06	…
	n_{tII}	0.246	0.304	0.248	…
	ε_{tII}	0.03	0.039	0.036	…
Region III	K_{tIII}	283.727	270.147	255.388	…
	n_{tIII}	0.308	0.3	0.281	…
Compression					
Region I	K_{cI}	193.019	203.517	209.894	244.287
	n_{cI}	0.146	0.138	0.123	0.139
	ε_{cI}	0.031	0.027	0.028	0.034
Region II	K_{cII}	337.909	354.487	354.977	426.972
	n_{cII}	0.303	0.29	0.268	0.302
	ε_{cII}	0.074	0.078	0.074	0.106
Region III	K_{cIII}	498.99	528.81	517.845	608.695
	n_{cIII}	0.455	0.446	0.414	0.456
Near-eutectic Al-Si alloy					
Tension					
Region I	K_{tI}	154.028	132.862	149.417	178.69
	n_{tI}	0.08	0.057	0.04	0.06
	ε_{tI}	0.006	0.004	0.004	0.007
Region II	K_{tII}	316.738	265.338	225.788	308.248
	n_{tII}	0.221	0.181	0.112	0.173
	ε_{tII}	0.018	0.011	0.008	0.034
Region III	K_{tIII}	522.637	586.949	434.71	291.541
	n_{tIII}	0.345	0.363	0.251	0.153
Compression					
Region I	K_{cI}	287.74	326.362	319.521	254.742
	n_{cI}	0.095	0.093	0.1	0.09
	ε_{cI}	0.025	0.021	0.025	0.021
Region II	K_{cII}	443.915	515.466	481.172	400.959
	n_{cII}	0.212	0.211	0.209	0.208
	ε_{cII}	0.086	0.069	0.072	0.063
Region III	K_{cIII}	538.518	717.629	615.602	556.288
	n_{cIII}	0.29	0.335	0.303	0.328
Hypereutectic Al-Si alloy*					
Compression					
Region I	K_{cI}	350.429	357.767	324.19	420.92
	n_{cI}	0.108	0.097	0.086	0.137
	ε_{cI}	0.028	0.028	0.018	0.05
Region II	K_{cII}	450.609	505.592	463.127	569.9
	n_{cII}	0.174	0.19	0.173	0.234
	ε_{cII}	0.074	0.071	0.06	0.11
Region III	K_{cIII}	384.68	537.403	513.57	500.495
	n_{cIII}	0.111	0.209	0.207	0.171

*No plastic region from tensile tests could be obtained to determine the Hollomon parameters
Different regions were identified by extrapolating the linear trend lines of two adjacent regions in Fig. 7(a) and taking their intersection points as a transition point between the two regions. These transitions are given by the symbol ε (strain) with appropriate suffixes in the table above. The range of strains can be obtained from the difference between two such adjacent ε values

to present these relationships empirically by employing, (i) exponential fit, (ii) linear fit, and (iii) power law fit, which could be useful for further analysis and application of binary Al-Si alloys. The equations for above three curve fittings along with the R^2 values obtained from these three types of plots are listed in tables within the inset of Fig. 8(b), and (c). Overall, the best curve fitting was obtained as an exponential function although there is no theoretical justification at this stage.
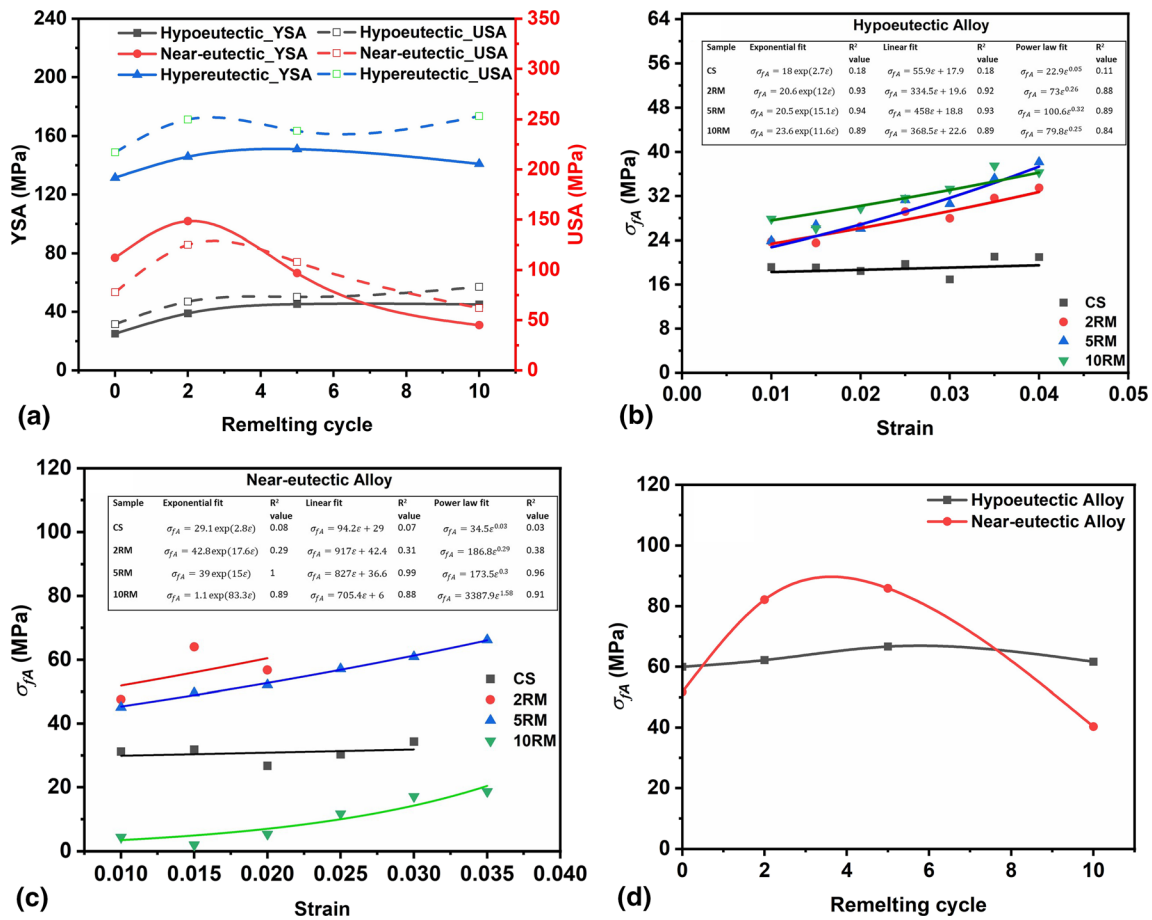
Fig. 8 Yield strength asymmetry (YSA) and ultimate strength asymmetry (USA = UCS—UTS) plots as a function of remelting cycle for different Al-Si alloys (a), (b,c) the flow asymmetry plots as a function of strain for hypoeutectic alloy (b), and near-eutectic alloy (c) along with the typical exponential curve fitting, (d) the flow asymmetry (between UTS and compressive stress at the corresponding uniform strain in tension) plot at the uniform strain level; also given in Fig. (b,c) are the equations of trend lines as inset table for the data points

The increase in flow stress asymmetry as a function of strain in Fig. 8(b), and (c), based on the best fitting of data (exponential fit as stated above), suggests a relationship of type:

$$\sigma_{fA} = pe^{q\varepsilon} \qquad \text{(Eq 3)}$$

where p and q are constants of exponential curves with their values ranging from 18.0 to 23.6 and 2.7 to 15.1, respectively, for hypoeutectic Al-Si alloys, and from 1.1 to 42.8 and 2.8 to 83.3, respectively, for the near-eutectic Al-Si alloys. The flow asymmetry was calculated by taking the difference between the UTS values (in tension) and flow stress values (in compression) corresponding to the uniform strain at UTS point. In Fig. 8(d), the flow asymmetry was plotted as a function of remelting cycle for hypoeutectic and near-eutectic Al-Si alloys. It is noted to vary with composition and remelting cycle to a different extent.

3.3 Asymmetry Factor (A.F.)

The asymmetry factor, which represents the degree of asymmetry, is the ratio of the difference in absolute values ($|\sigma_{cy}| - |\sigma_{ty}|$) between compressive yield strength ($|\sigma_{cy}|$) and tensile yield strength ($|\sigma_{ty}|$) to the average ($|\sigma_{cy}| + |\sigma_{ty}|$)/2 of the two (Ref 37).

$$AF_y = \frac{(|\sigma_{cy}| - |\sigma_{ty}|)}{(|\sigma_{cy}| + |\sigma_{ty}|)/2} \qquad \text{(Eq 4)}$$

The asymmetry factor (AF_y) was calculated at the yield point for all the compositions and for different remelting cycles. The asymmetry factor initially increased up to two remelting cycles, but it appeared to remain constant for further remelting cycles, especially in the hypoeutectic and hypereutectic Al-Si alloys; a significant change could, however, be observed in the near-eutectic Al-Si alloys, Fig. 9.

3.4 Relation Between Microstructure and Mechanical Properties

Different aspects of microstructure, including the grain size (d), under different conditions, are described elsewhere (Ref 48). As elaborated earlier (Ref 48), the measurements of the grain size and volume fraction of silicon particles were done by using mean linear intercept method and areal fraction measurement programs, respectively, built in the image analysis process in Leica microscope. Also, presented earlier (in Ref. 48, Fig. 4a-d), are: the volume fraction of phases (a), GS (grain size) (b), SDAS (secondary dendrite arm spacing) (c), and primary Si size (d), as a function of silicon content for different remelting cycles. With increasing Si in binary Al-Si alloys, the proportion of eutectic phase increases by sharing with the existing matrix Al-phase. Beyond the eutectic composition, the increasing Si starts to exist in the form of primary Si particles. Similarly, the Si particles get redistributed with increasing

number of remelting cycles to form more eutectic phase proportion. Consequently, the matrix grain size also decreases with increasing Si content and remelting cycle. The effects of various microstructural parameters on tensile and compressive properties were examined here. The effects of volume fraction of the eutectic phase (EP) are presented in Fig. 10(a)-(d), whereas the effect of grain size is elaborated in Fig. 11(a)-(d).

From the tensile test data, the TYS and UTS were found to first increase with increasing volume fraction of the eutectic phase, from hypoeutectic to near-eutectic composition, but then the same decreased for the hypereutectic composition, Fig. 10(a). This variation in TYS and UTS as a function of eutectic phase proportion is similar to the trend observed in Fig. 4(a), which exhibits the variation as a function of Si content. Figure 10(b) shows a decrease in elongation with increasing eutectic phase fraction in the Al-Si alloys, irrespective of the remelting cycle. In Fig. 10(c), the CYS increases with the increase in eutectic phase proportion which is opposite to the trend shown for elongation in Fig. 10(b). Such variations in properties with the eutectic phase are expected because the eutectic phase proportion itself increases with increasing Si content, Fig. 10(d). The trend lines suggested by data are represented by equations as inset in Fig. 10(b)-(d).

Flow stresses ($\sigma(\varepsilon)$) at selected constant strain levels (ε), including the yield strength (YS represented by symbol σ_y here), were plotted, as shown in Fig. 11(a)-(c), as a function of the inverse square root of grain size (d) in the form of a Hall–Petch (H-P) type relationship (Ref 51-53),

$$\sigma(\varepsilon) = \sigma_0(\varepsilon) + k(\varepsilon)d^{-0.5} \qquad (Eq\ 5)$$

where $\sigma_0(\varepsilon)$ and $k(\varepsilon)$ are the Hall–Petch parameters. Different grain sizes were taken from different remelting cycles for each composition.

The Hall–Petch type plot, $\sigma(\varepsilon)$ versus $d^{-0.5}$, made from tensile test data did not follow this relationship. However, from compression tests, the H-P type plot seems to be supported, within a large scatter in the data, as shown in Fig. 11(a) for hypoeutectic and Fig. 11(b) for hypereutectic Al-Si alloys. It is noted that for an unknown reason, the large scatter is caused by the data of compression sample of two remelting cycle. The trend lines including the data point of two remelting cycle and by excluding the data of 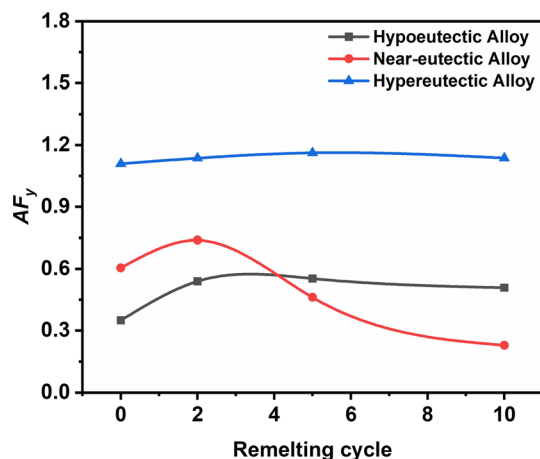two remelting cycle are shown by dash lines and solid lines, respectively. The H-P type plot made from compression tests for all the alloys together (for different alloy compositions and remelting cycles) is shown in Fig. 11(c) for compressive yield strength (at 0.2% plastic strain) and flow stresses at strain levels of 5% and 10%. The variations in σ_0 and k as a function of strain are plotted in Fig. 11(d) by including the H-P parameters at these and other strains, whose H-P plots are not presented here.

The Hall–Petch parameters σ_0 (intercept) and k (slope) are given as inset in Fig. 11(a) and (b) in the form of H-P relationships along with the trend lines. The comparison of these parameters between hypoeutectic and hypereutectic Al-Si alloys can be summarized as follows. The values of σ_0 are found to be higher in hypereutectic Al-Si alloy than that in the hypoeutectic Al-Si alloy. On the other hand, the values of k are higher in hypoeutectic alloy than that in the hypereutectic Al-Si alloy. The Hall–Petch parameters σ_0 (intercept) and k (slope) are constants, which are independent of grain size. With the more amount of silicon present in the hypereutectic Al-Si alloy, it is expected that the strengths of both the grain interior (σ_0) and grain boundaries (k) should be higher than that in the hypoeutectic alloy. This appears to be true for σ_0 values. However, the presence of silicon in the grain boundary might destabilize the grain boundary structure and make it more open to reduce grain boundary strengthening component. Under this presumption, the higher silicon present in the grain boundaries of hypereutectic alloy may cause reduction in the grain boundary strengthening (k) of this alloy.

It is seen that while the σ_0 decreases with increasing strain, at smaller strains, k is noted to show the opposite trend. At larger strains, σ_0 increases rapidly with increasing strain, whereas k reaches saturation level but with a slight indication of decline at still higher strain levels. The effect of strain on σ_0 and k can be expressed by Eqs 6a, b and 7a, b, respectively.
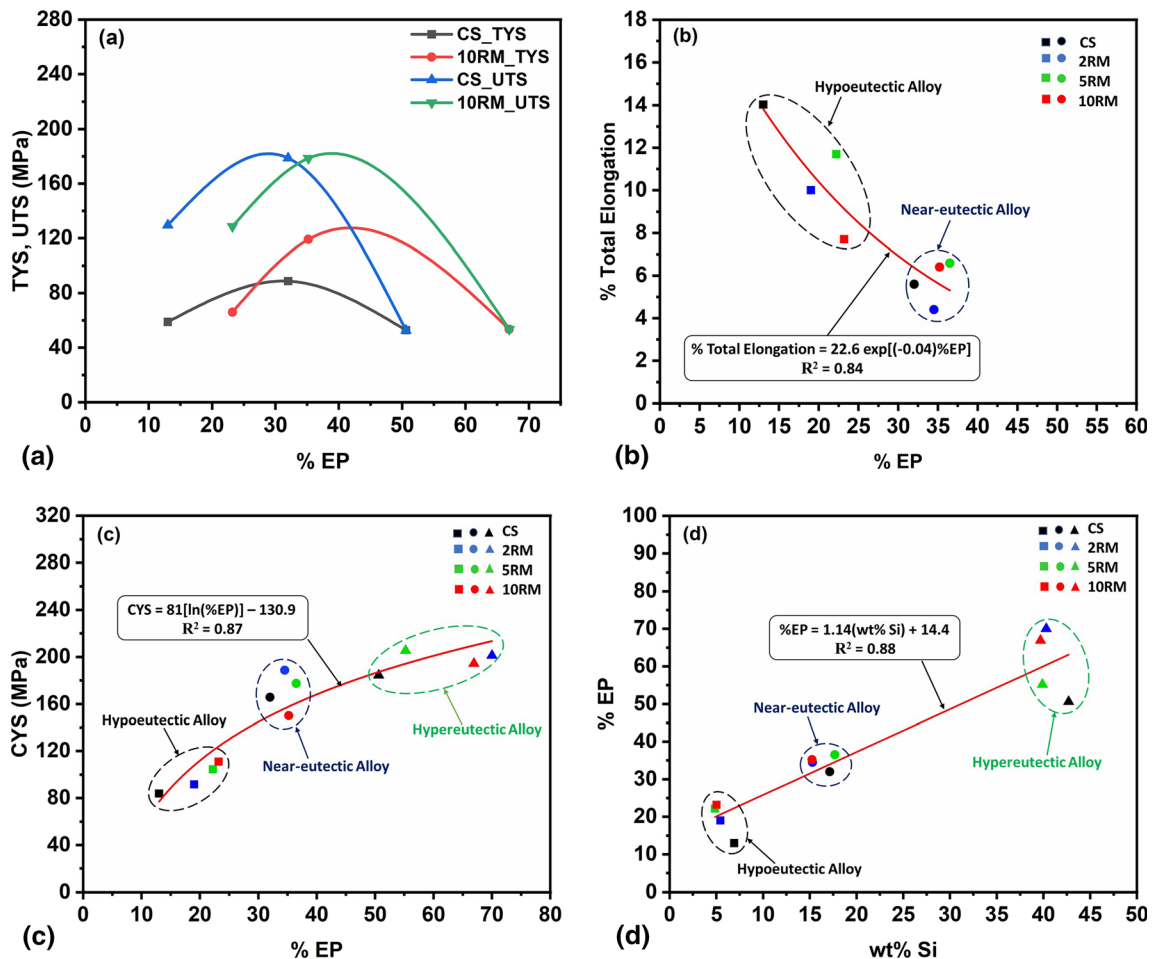
$$\sigma_0 = -562.1\varepsilon + 13.4,\ R^2 = 0.87 \qquad (Eq\ 6a)$$

$$\sigma_0 = 568.4\varepsilon - 24.3,\ R^2 = 0.98 \qquad (Eq\ 6b)$$

$$k = 113.6\ln(\varepsilon) + 1355,\ R^2 = 0.97 \qquad (Eq\ 7a)$$

$$k = -936.8\varepsilon + 1083,\ R^2 = 0.94 \qquad (Eq\ 7b)$$

The Hall–Petch plots at different strain levels (typically shown in Fig. 11(c) at three strain levels 0.2%, 5%, 10% with $R^2 = 0.83$, 0.83, 0.8, respectively) exhibit the H-P parameters σ_0 and k to vary with strain as illustrated in Fig. 11(d). By considering the existing theories of Hall–Petch relationship (Ref 54), the following hypothesis emerges to explain the trend of decrease and increase in σ_0 and the increase and then decrease in k. In the lower strain range, the decrease in σ_0 (Eq 6a) and increase in k (Eq 7a) with increasing strain suggest that the dislocations generated at one grain boundary are able to travel to the opposite grain boundary and get impeded there during deformation. This means that the grain boundary resistance becomes stronger by dislocation pile-up, and at the same time the back stress arising from these dislocations causes the grain interior to be softer. The softening of grain interior may be expected to occur when the dislocations inside the grain, coming from different sources, mutually get annihilated with increasing strain. On the other hand, as the strain

Fig. 9 Plot of asymmetry factor as a function of remelting cycle for hypoeutectic, near-eutectic, and hypereutectic Al-Si alloys

Fig. 10 Variation in tensile properties: (a) TYS and UTS, (b) total elongation, and (c) CYS as a function of the volume fraction of the eutectic phase (EP), which, in turn, is related to Si content (d)

increases, the increasing dislocation density may facilitate formation of substructure like cell and subgrains which may cause increasing σ_0 (Eq 6b), but the lower resistance of their cell boundaries may contribute to overall decrease in the k (Eq 7b) value.

3.5 Fractography

Fractographs obtained upon tensile tests are arranged in Fig. 12 to show the effects of Al-Si alloy composition along the row (horizontally) and the remelting cycle along the column (vertically). In Fig. 12(a),(b),(c), and (d), the dimple type fracture mode is exhibited under tensile loading in hypoeutectic Al-Si alloys, whereas, in hypereutectic Al-Si alloys, the cleavage or quasi cleavage type fracture mode is observed, Fig. 12(i),(j),(k), and (l). A mixed fracture mode, the combination of dimple and cleavage failure mode, can be seen in near-eutectic Al-Si alloys, Fig. 12(e),(f),(g), and (h).

4. Discussion

Al-Si alloys investigated here show distinct microstructures, Fig. 1, and mechanical properties as a function of composition and remelting cycle, Fig. 2, 3, 4, 5, 6, 7, 8, 9, 10. Tensile stress–strain curves for the same composition and condition show

lower flow stress and fracture/maximum strain than that of the corresponding compressive stress–strain curves, Fig. 3 and Table 3. This led to some understanding of asymmetry in property and the development of quantitative process–structure–property relationships. Discussed below are certain interesting aspects of these structure–property relationships which need further elaboration.

4.1 Source of Strengthening and Failure

As seen in Fig. 1, the microstructures consist of α-Al, eutectic Al-Si phase, and primary Si particles of varying proportion and morphology depending on composition and remelting cycle. These phases are known to have different properties. For example, the hardness values from the literature (Ref 55-57) and also that measured by the present authors (Ref 48) are reported to be 30-40, 60-70, and 400-1000 HV, respectively. The contributions to the strengths of present alloys in the as-cast stage come from solid solution strengthening, precipitation, particle hardening, grain/interphase boundary strengthening, two-phase and composite type strengthening, substructure strengthening, etc. The associated mechanisms and the measure of their effects on strengthening are well investigated and reported in the literature (Ref 58, 59). Plastic deformation of as-cast Al-Si alloys will contribute to further strengthening through interaction between dislocations and the prior existing microstructural features.
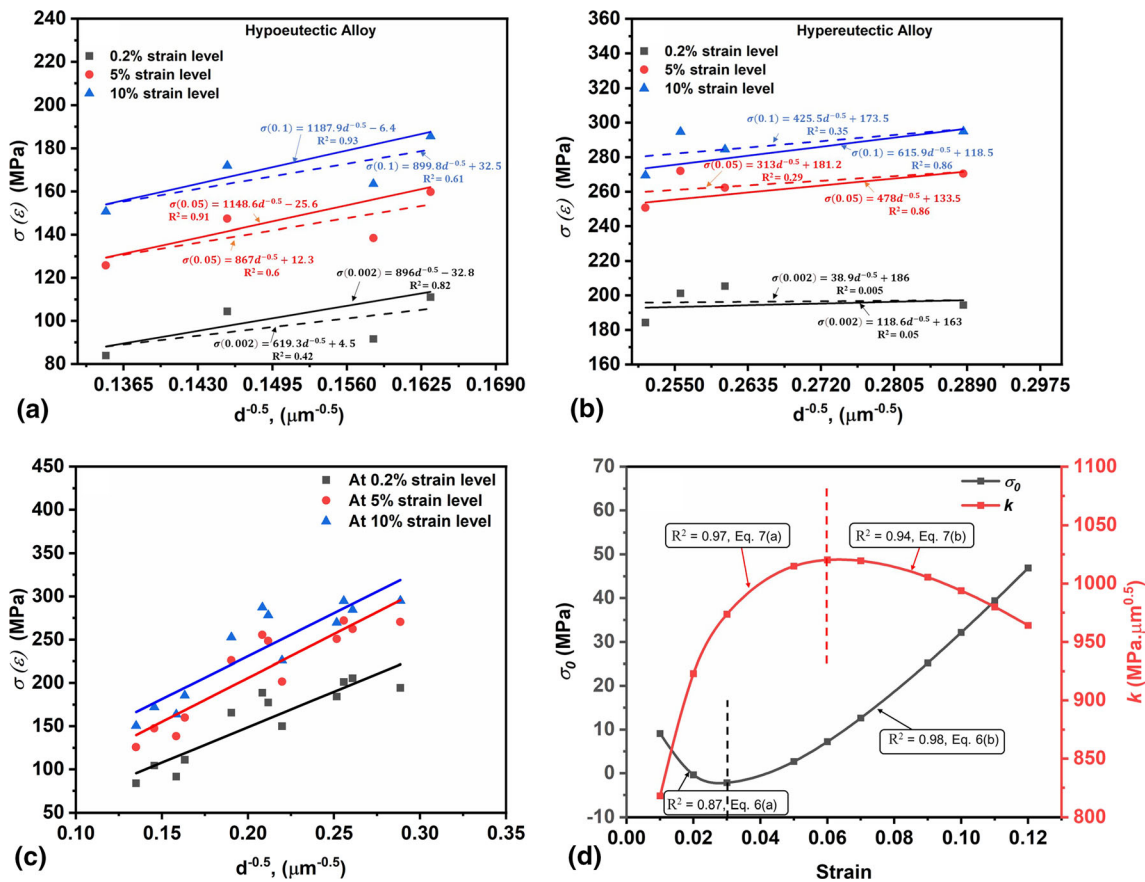
Fig. 11 (a,b,c) Hall–Petch type plots at selected strain levels (proof stresses at 0.2% (yield point), 5%, and 10% strains) for: (a) hypoeutectic Al-Si alloy, (b) hypereutectic Al-Si alloy, (c) all Al-Si alloys and remelting cycles; (d) variation in H-P parameters σ_0 and k from (c) as a function of strain along with that at other strain levels not plotted in (c); in Fig. (a,b) the H-P relationships (trend lines along with adjacent equations) are given by dashed lines based on all four data points, whereas the same, after excluding the data point of two remelting cycle, are given by solid lines

The nature of stress–strain curves depends not only on deformation behavior but also on fracture behavior of the constituents/phases present in the material being deformed. While the ductile materials are dominated by plastic deformation, the brittle material can be taken over by fracture even prior to plastic deformation can set in. The stress–strain curves from tensile tests, Fig. 2(a-c), suggest that hypereutectic alloy is not able to deform plastically because it contains ~ 30 vol% primary silicon and ~ 50 vol% eutectic (α-Al + Si) phase, whereas the deformable α-Al is only in limited (20-30%) fraction surrounded by the former two phases. Plastic deformation would necessitate the deformation or compatibility of the coexisting phases. This does not seem to be satisfactory because the soft α-Al is dispersed as islands in the eutectic phase, whereas the hard Si exists as large particles that inhibit deformation. However, the increased volume fraction of the α-Al phase, in near-eutectic and hypoeutectic compositions, is able to deform to a limited extent. This may be possible because the eutectic phase, earlier resisting the plastic deformation, may become compatible to deformation. The deformable phase undergoes work hardening during plastic deformation, and if its strength in this process matches with that of the coexisting harder phase, then both phases may contribute to further deformation. In the hypoeutectic composition, the large proportion of soft α-Al (85-90 vol%) phase may be helping through such compatibility to exhibit signif-

icant plastic strain of the material. In the case of near-eutectic composition, the deformable soft phase becomes less (55-60 vol%), whereas the proportion of the eutectic phase (30-40 vol%) becomes larger. Because of this, the tensile elongation also becomes less. The fracture caused with no plastic strain during deformation of hypereutectic alloy exhibits cleavage type fracture owing to the presence of large Si particles and their more volume fraction, Fig. 12. On the other hand, the hypoeutectic and near-eutectic alloys, which show some plastic deformation prior to fracture, exhibit a combination of ductile and brittle fracture.

An attempt to quantitatively relate tensile properties with composition and remelting cycle through the microstructure evolved led to interesting results in some aspects but not in other aspects. No systematic effect of grain size was found on yield strength, tensile strength, and elongation, the possible reason for which could be due to the dominant effect of other factors like other phases, their morphology, their role as a barrier to deformation, etc. It is known that with increasing Si in Al-Si alloy, the proportions of eutectic phase and Si particles increase with a simultaneous reduction in grain size of the α-Al matrix phase. But, they do not allow this α-Al phase to deform as polycrystalline without influencing the nature of grains. In fact, the tensile properties plotted in Fig. 10(a), and (b) rather suggest that the linearly increasing volume fraction of the eutectic phase with increasing Si content, Fig. 10(d), is more
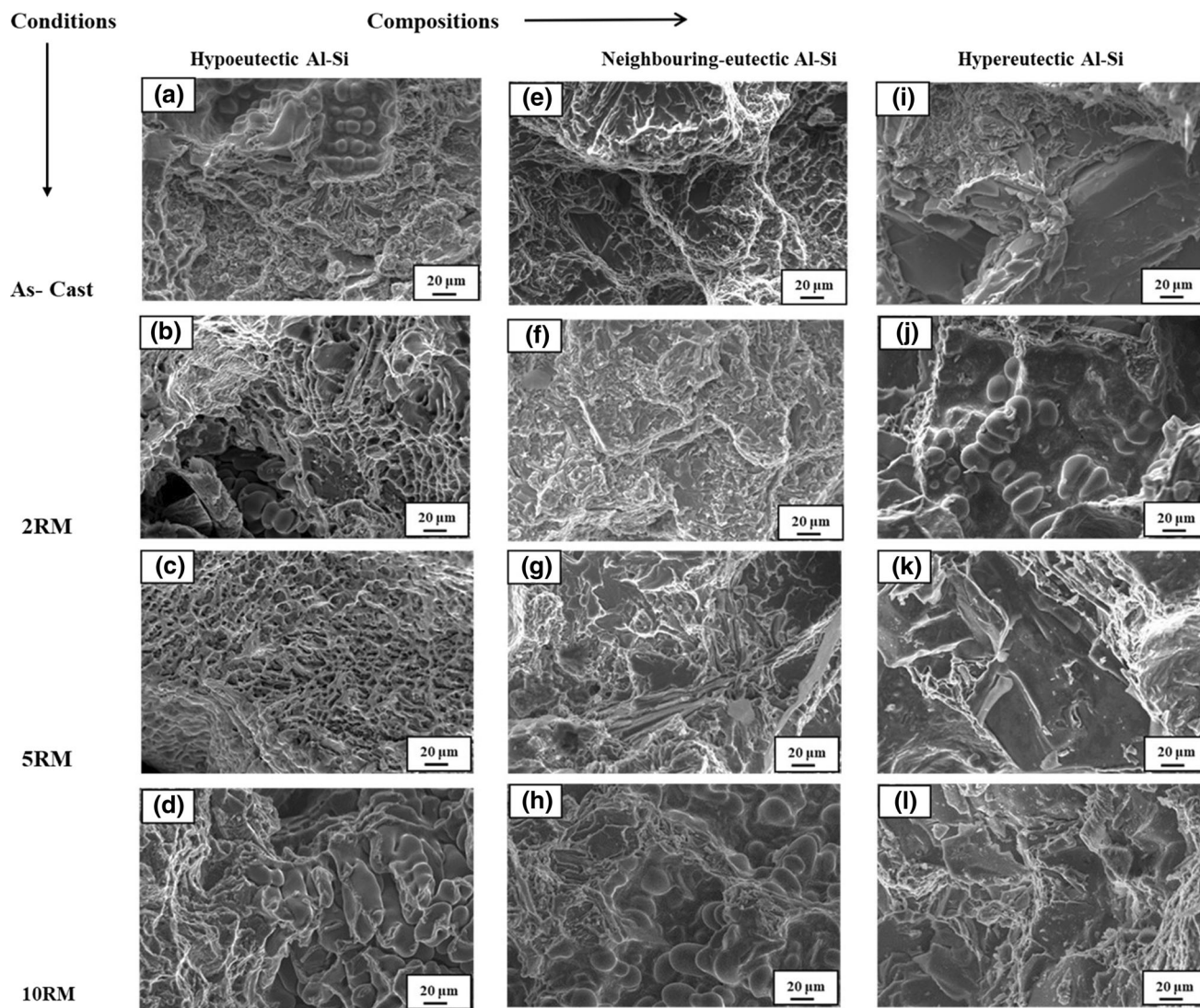
Fig. 12 SEM fractographs upon tensile tests of the Al-Si alloys of different compositions and for different remelting cycles

pertinent here to relate to tensile properties. The occurrence of an increase in TYS and UTS from hypoeutectic to the near-eutectic alloy can be understood, as discussed above, due to the increasing fraction of nearly comparable (although a little harder) second phase rather than the very hard Si phase. However, once the proportion of the hard Si phase increases, then the material is not able to deform plastically, in which case it fractures, and it is only notional to call it TYS and UTS. The decrease in total elongation with an increasing proportion of the eutectic phase can be associated with the role of the eutectic phase as a barrier to continued plastic deformation.

In contrast with the tensile deformation behavior, as expected for brittle materials like the present Al-Si alloys of different compositions, the compressive flow curves show significant improvement in deformability, Fig. 2(d-f) and Fig. 3(a), (b). The following probable explanations for the improved deformability, with larger engineering strain and simultaneous strengthening, in compression, are suggested. (i) During compression, the presence of casting defects like pores, micro-cracks, etc. may get closed by the movement of materials toward each other from the opposing surfaces of these defects. The reverse is true in tensile deformation, whereby the cracks can further open up in the loading direction along with the crack tip propagation at a right angle to the loading direction. (ii) In the present material, the deformable α-Al phase can undergo plastic deformation, whereas the hard Si particles may slide, with the eutectic phase providing local deformation to maintain compatibility among different phases. This process may get more and more facilitated as the cross-sectional area increases in compression tests, whereas the reduction in cross-sectional area in tension may either cause exhaustion of plastic deformation of softer α-Al phase or bring the harder sliding Si particles together. Such a development of dynamic heterogeneity may cause necking and failure during tension tests. (iii) There occurs change in grain shape of polycrystalline material during diffusion creep [58]. In tensile deformation, the grains get elongated in loading direction and partially account for the elongation of sample. Under compressive diffusion creep, the same grains get flattened and account for the change in the shape of compression sample. The material flow during present study is suggested to be analogous to this but by multiple slip processes. This is exhibited through the reduction in the cross-sectional area of specimens in tensile deformation and an increase in the cross-section area in compression. Even in

conventional test condition, deformation in tension becomes constrained for material flow by the geometry and progressively reducing gage cross-sectional area of the specimen. In contrast, in compression, the configuration becomes opposite, and as such the open end of specimen facilitates material flow owing to the unconstrained condition.

In the present alloys, although even the hypereutectic alloy exhibited significant deformation in compression, the failure occurred catastrophically to support the brittle fracture. No fracture occurred during compressive deformation of hypoeutectic and near-eutectic alloys till maximum strains of 35-40% (not shown in the stress–strain curves).

4.2 Significance of Flow Asymmetry and Structure-Property Relationships

Al-Si alloys investigated here exhibit asymmetry between tensile and compressive yield strengths and other flow properties, as presented in the section on results. Noticeable among them are illustrated in Fig. 6, 8, 9, viz. for asymmetry in work hardening rate in Fig. 6, for asymmetry in Hollomon parameters in Fig. 7, for flow stress asymmetry in Fig. 8, and for asymmetry factor in Fig. 9. The results on asymmetry reported in a few materials are summarized in Table 5, along with the source of asymmetry.

Primarily, asymmetry in yield strength has been extensively studied in hcp metals, e.g., Mg-alloys (Ref 12-17) and Ti-alloys (Ref 18-20), fcc metals Ni-superalloys (Ref 21-23), and Al-alloys (Ref 28-31). In hcp metals like Mg, tensile twinning occurring in compression tests but not in tensile tests causes asymmetry; any factor like grain refinement fine precipitates which suppress twinning or reduce its volume fraction rather eliminates asymmetry (Ref 16). In Ti-alloys (Ref 18), higher compressive yield strength was attributed to the presence of texture, which increases the critical resolved shear stress for deformation. Tsuno et al. (Ref 22) investigated the source of tension compression yield asymmetry in Ni-based superalloys. Tension–compression asymmetry was observed only in the superalloy where dislocation cross-slip was restricted, but the mechanical twinning was formed. The inhibition of dislocation cross slip makes deformation by slip process difficult, but the concurrently arising stress concentration can trigger twin development. Therefore, the asymmetry was attributed to the formation of micro-twins. The mechanism of micro-twin formation is elaborated elsewhere (Ref 60). In A356 aluminum alloy, the source of asymmetry is ascribed to the role of micron size particles and nanosized precipitates acting as sites for cavity nucleation in tensile deformation but not in compression. Tension–compression asymmetry was reported from the in-plane stress states in cylindrical cup drawing of AA2090 Al-alloy in (Ref. 29). The magnitudes of asymmetry factor (AF) for different materials as determined by Eq 4 are listed in Table 5. It is seen that magnitude of AF varies from 0.09 to 0.52 in Mg-alloys depending on composition, whereas it is 0.05 to 0.09 in Ti-alloys. Similarly, AF is 0.08 in Ni-superalloy and 0.12 in AA2090, and 0.14 in A356 Al-alloys. As compared to these values of asymmetry, AF in the present work is seen to vary from 0.23 to 1.16 depending on Si content in the Al-Si alloys; the Al-rich composition shows lower values, whereas the dominance of Si in the composition leads to higher values. These values are as high as or even greater than that of the Mg alloys. Some variations in AF observed here could have their origin in the reasons given earlier (Sect. 4.1.) for the difference

in flow properties between tensile versus compressive deformation. Furthermore, the Si of the diamond cubic crystal structure is reported to exhibit different elastic properties in different directions (Ref 61), the presence of which in the Al-Si alloys may control the deformation behavior of otherwise isotropic aluminum matrix. This could be the reason that the asymmetry also increases from the hypoeutectic to hypereutectic alloy compositions.

The plot of the work hardening rate of continuous decrease in θ at the beginning of plastic deformation supports stage III of dominating dynamic recovery behavior. Although the flow stress in compression is more than that in tension, the reverse is true for the variation in θ as a function of strain. This suggests that continuing deformation in tension is achieved by rapid generation of dislocations and simultaneous hindrance of their mobility, which together promote dynamic recovery to lead to a rapid drop in work hardening rate. Later, the barrier to dislocation motion starts dominating and causes the tensile specimen to undergo failure. On the other hand, in compression, plastic deformation continues through the prolonged generation of dislocations and their favorable redistribution to continue gradual dynamic recovery. As a consequence of this, the plot of θ shows a crossover of the compressive θ-ε curve by the tensile θ-ε curve. Beyond this intersection point, while the magnitude of θ continues to drop up to failure during tensile deformation, θ in compression attains a constant value. This saturation in θ with increasing strain supports the stage IV behavior of work hardening, where the generation of dislocations is slowed down, but deformation can continue through large obstacle-free slip distance and the occurrence of cross-slip (Ref 62, 63). The difference in θ-ε curves between tension and compression is more in near-eutectic alloy than that in hypoeutectic alloy. The intersection point of tensile-compressive θ-ε curves appears at a smaller strain ($\varepsilon \sim 0.035$) for hypoeutectic alloy than that for the near-eutectic alloy ($\varepsilon \sim 0.05$). Similarly, this transition strain is reduced by increasing the remelting cycle, e.g., from $\varepsilon \sim 0.035$ to 0.02 for hypoeutectic alloy and from $\varepsilon \sim 0.05$ to 0.025 for near-eutectic alloy. The difference in flow properties, including the nature of σ-ε and θ-ε curve, suggests the asymmetry to be influenced by the presence of Si particles and remelting cycle; asymmetry increases with increasing Si content and reducing grain size, by remelting.

Flow properties of the present alloys were shown to vary as a function of the composition, remelting cycle (Fig. 2, 3, 4, 5, 6, 7, 8, 9, 10), and a number of microstructural features which include eutectic phase fraction (Fig. 10), grain size (Fig. 11). Surprisingly, the H-P relation is shown to be obeyed based on the compression test, Fig. 11, but not in the tension test. It may be noted that with increasing Si, the proportion of the eutectic phase increases, and simultaneously, the grain size decreases, both of which are known to increase the strength of the present alloy. In order to examine whether the inter-particle spacing (Λ), which involves the size and volume fraction of the second phase particle, might be a suitable parameter, an attempt was made to relate the yield strength with Λ(Ref 64). $\Lambda$is given by,
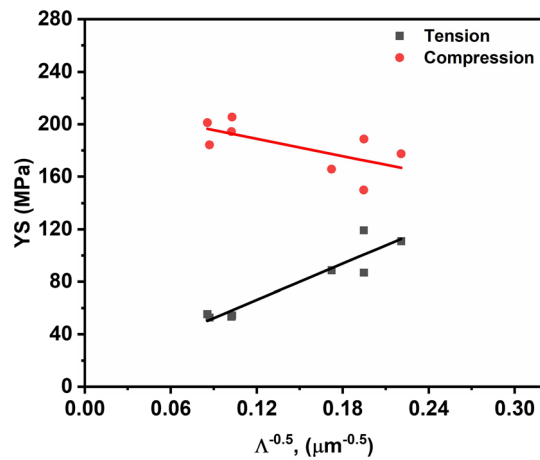
$$\Lambda = \left(1.23\sqrt{\frac{2\pi}{3f_p}} - 2\sqrt{\frac{2}{3}}\right)(l/2) \quad \text{(Eq 8)}$$

where f_p is the volume fraction of Si particles and l is the length of the primary silicon, which is taken to represent the particle diameter. Given in Fig. 13 is the plot of YS versus $\Lambda^{-0.5}$ in

Table 5 Summary of tension−compression asymmetry (TCA), including asymmetry factor (AF), in metals with hcp and fcc crystal structures

Alloy		TYS, MPa	CYS, MPa	TCA	AF	Suggested reason/effects on asymmetry	Ref
Mg-based Alloys	Mg Alloy (Mg-Zn-Y-Zr)	231	211	20	− 0.09	Twinning	[12]
	AZ31 Mg Alloy	200	125	75	− 0.46	Texture and twinning	[14]
	AZ31B-O	181	106	75	− 0.52	Twinning	[15]
	Mg-Zn-Ca alloy	178	138	40	− 0.25	Grain size, texture, Twinning	[16]
Ti-based Alloys	Ti-5Al-3Mo-1.5 V	980	1070	90	0.08	Heat treatment	[18]
	Ti-6.6Al-3.3Mo-1.8Zr-0.29Si	930	1000	70	0.07	Strain rate	[19]
	Ti-6242	931	982	51	0.05	Type of dislocation slip	[20]
Ni-based Alloy	Ni-superalloy	1080	1000	80	− 0.07	Micro-twin formation, Temperature	[22]
Al-based Alloys	AA2090	279.62	248.02	31.6	− 0.12	Void-crack nucleation	[29]
	A356	329	378	49	0.14		[30]
Hypoeutectic Al-Si alloy	0	58.9	83.9	25	0.35	During loading, Si shows the anisotropic nature and Al matrix shows the isotropic nature	Present work
	2	52.7	91.6	38.9	0.54	Incompatibility during deformation between the phases	
	5	59.2	104.4	45.2	0.55	Possibility of presence of pores, cracks/voids	
	10	66	111	45	0.51		
Near-eutectic Al-Si alloy	0	88.7	165.6	76.9	0.60		
	2	86.9	188.7	101.8	0.74		
	5	110.9	177.4	66.5	0.46		
	10	119.2	150	30.8	0.23		
Hypereutectic Al-Si alloy	0	52.8	184.3	131.5	1.11		
	2	55.4	201.2	145.8	1.14		
	5	54.4	205.4	151	1.16		
	10	53.5	194.4	140.9	1.14		

Fig. 13 Hall–Petch type plot of yield strength and interparticle spacing in tension and compression for near-eutectic and hypereutectic alloys
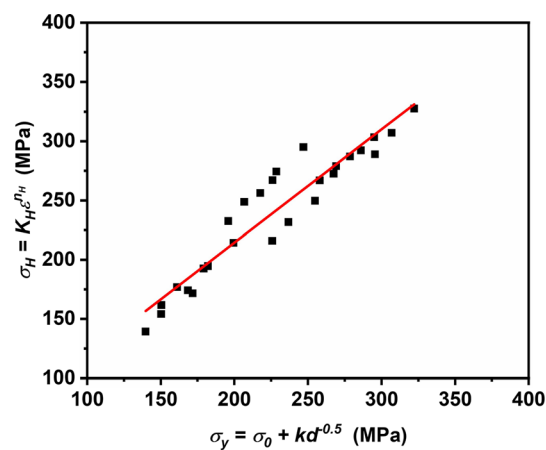
Fig. 14 Comparison of flow stresses calculated by using Hollomon and Hall–Petch parameters for compression test

tension and compression. Interestingly, the H-P type relationship appears to be reasonably obeyed by considering the yield strength in tension but not in compression. In fact, the compressive yield strength decreases as Λ decreases.

This observation further suggests a requirement of closely examining the interfacial phenomena between dissimilar phases, which in this case are Al (α) matrix and Al-Si eutectic or Si particles with anisotropic elastic properties. It appears that the orientation of Si particles and the Al-Si interphase play an important role by creating local (in the vicinity of interphase) variations in the stress-state differently during tensile and compressive deformation. This effect is also reflected in the values of Hollomon parameters obtained from tensile and compressive tests, Table 4, Fig. 7. Probably, the occurrence of different stages in the Hollomon plot represents different stages of micro-mechanisms for deformation. Since the flow stress increases with increasing strain and decreasing grain size, the effects of straining and grain size could be combined to understand the strengthening of this alloy. The Hall–Petch relationship was derived by employing the concept of geometrically necessary dislocations while using the work hardening based model for polycrystalline strengthening (Ref 65). While Fig. 7 shows stress–strain curves re-plotted in the form of

Hollomon relationship, the H-P type plot in Fig. 11 shows the effect of grain size on flow stress at different strain levels. The importance of work hardening and polycrystalline strengthening is mutually related from the analysis of stress–strain curves for different compositions and remelting cycles as reproduced in Fig. 14.

5. Conclusions

Room temperature tensile and compressive deformation behavior of Al-Si alloys was found to depend on microstructure developed as a function of chemical composition and remelting cycle, as summarized below.

1. Microstructures of Al-Si alloys of hypoeutectic, near-eutectic, and hypereutectic compositions reveal that the grain size decreases, whereas the silicon particle size increases with increasing silicon content.
2. In tension, the yield strength first increases and then decreases with increasing silicon content from the hypoeutectic to hypereutectic Al-Si alloy. In compression, the yield strength is found to increase first rapidly and then marginally with increasing silicon content.
3. Stress–strain curves in compression exhibit higher flow stress and deformability than that in tension in all conditions of composition and remelting cycle. The nature of stress–strain curves can be expressed by Hollomon type relationships. The associated work hardening follows stage III behavior in tension and stage III and IV behavior during compressive deformation.
4. The tension–compression flow asymmetry increases as a function of increasing silicon and strain, whereas no systematic variation is evident as a function of remelting cycle.
5. The variation in flow stress as a function of grain size in compression is noted to follow the Hall–Petch type relationship of increasing strength with decreasing grain size. However, no such effect of grain size could be found in tensile deformation, but the variation in yield strength was found to be systematic as a function of interparticle spacing, which can be expressed by the Hall–Petch type relationship.
6. A comparison of initial microstructures and fractographs obtained from tensile specimens suggests that the fracture mode changes from ductile to cleavage fracture with the increasing silicon content. However, in low silicon alloys, the grain refinement with an increasing remelting cycle contributes to ductile fracture with an increasing proportion of dimple formation.
7. The Hollomon type relationship and Hall–Petch type relationship, obtained from stress–strain curves of the compression tests in Al-Si alloys studied, appear to suggest that there exists a linear interrelationship between the work hardening and grain boundary strengthening.

Bhabha Atomic Research Centre, Mumbai, for their help in providing the compositional analysis of the present material.

References

1. J. Campbell, Complete Casting Handbook: Metal Casting Processes, Metallurgy, Techniques and Design: Second Edition. 2015. https://doi.org/10.1016/C2014-0-01548-1

2. J. R. Davis, *ASM Handbook of Aluminum and Aluminum Alloys*. 1993

3. K. Li, J. Zhang, X. Chen, Y. Yin, Y. He, Z. Zhou, and R. Guan, Microstructure Evolution of Eutectic Si in Al-7Si Binary Alloy by Heat Treatment and its Effect on Enhancing Thermal Conductivity, *J. Mater. Res. Technol.*, 2020, **9**(4), p 8780–8786

4. V.C. Srivastava, R.K. Mandal, and S.N. Ojha, Microstructure and Mechanical Properties of Al-Si Alloys Produced by Spray Forming Process, *Mater. Sci. Eng. A*, 2001, **304–306**(1–2), p 555–558. https://doi.org/10.1016/S0921-5093(00)01514-8

5. D.K. Dwivedi, R. Sharma, and A. Kumar, Influence of Silicon Content and Heat Treatment Parameters on Mechanical Properties of Cast Al-Si-Mg Alloys, *Int. J. Cast Met. Res.*, 2006, **19**(5), p 275–282. https://doi.org/10.1179/136404606X153867

6. H.R. Ammar, C. Moreau, A.M. Samuel, F.H. Samuel, and H.W. Doty, Influences of Alloying Elements, Solution Treatment Time and Quenching Media on Quality Indices of 413-type Al-Si Casting Alloys, *Mater. Sci. Eng. A*, 2008, **489**(1–2), p 426–438. https://doi.org/10.1016/j.msea.2007.12.032

7. P. Ma, Y. Jia, K.G. Prashanth, Z. Yu, C. Li, J. Zhao, S. Yang, and L. Huang, Effect of Si Content on the Microstructure and Properties of Al-Si Alloys Fabricated Using Hot Extrusion, *J. Mater. Res.*, 2017, **32**(11), p 2210–2217. https://doi.org/10.1557/jmr.2017.97

8. T. Kimura and T. Nakamoto, Microstructures and Mechanical Properties of A356 (AlSi7Mg0.3) Aluminum Alloy Fabricated by Selective Laser Melting, *Mater. Des.*, 2016, **89**, p 1294–1301. https://doi.org/10.1016/j.matdes.2015.10.065

9. Y. Wang, H. Liao, Y. Wu, and J. Yang, Effect of Si Content on Microstructure and Mechanical Properties of Al-Si-Mg Alloys, *Mater. Des.*, 2014, **53**, p 634–638. https://doi.org/10.1016/j.matdes.2013.07.067

10. S.P. Nikanorov, M.P. Volkov, V.N. Gurin, Yu.A. Burenkov, L.I. Derkachenko, B.K. Kardashev, L.L. Regel, and W.R. Wilcox, Structural and Mechanical Properties of Al-Si Alloys Obtained by Fast Cooling of a Levitated Melt, *Mater. Sci. Eng. A*, 2005, **390**(1–2), p 63–69. https://doi.org/10.1016/j.msea.2004.07.037

11. M. Gupta and S. Ling, Microstructure and Mechanical Properties of Hypo/Hyper-Eutectic Al-Si Alloys Synthesized Using a Near-Net Shape Forming Technique, *J. Alloys Compd.*, 1999, **287**(1–2), p 284–294. https://doi.org/10.1016/S0925-8388(99)00062-6

12. X. Wang, W. Chen, M. Yang, J. Pan, D. Fang, J. Duan, W. Zhang, and W. Wang, Improving Tension/Compression Asymmetry of a Hot-Extruded Mg-Zn-Y-Zr Alloy Via Yttrium Addition, *Adv. Eng. Mater.*, 2021, **23**(9), p 1–10. https://doi.org/10.1002/adem.202100087

13. Y.Q. Chi, X.H. Zhou, X.G. Qiao, H.G. Brokmeier and M.Y. Zheng, Tension-Compression Asymmetry of Extruded Mg-Gd-Y-Zr Alloy with a Bimodal Microstructure Studied by In-Situ Synchrotron Diffraction, *Mater. Des.*, 2019, **170**, p 107705. https://doi.org/10.1016/j.matdes.2019.107705

14. J.B. Lin, W.J. Ren, X.Y. Wang, and L.F. Ma, Tension–Compression Asymmetry in Yield Strength and Hardening Behaviour of As-Extruded AZ31 Alloy, *Mater. Sci. Technol. (United Kingdom)*, 2016, **32**(18), p 1855–1860. https://doi.org/10.1080/02670836.2016.1149293

15. P. Zhou, E. Beeh, and H.E. Friedrich, Influence of Tension-Compression Asymmetry on the Mechanical Behavior of AZ31B Magnesium Alloy Sheets in Bending, *J. Mater. Eng. Perform.*, 2016, **25**(3), p 853–865. https://doi.org/10.1007/s11665-016-1961-3

16. L.B. Tong, M.Y. Zheng, S. Kamado, D.P. Zhang, J. Meng, L.R. Cheng, and H.J. Zhang, Reducing the Tension-Compression Yield Asymmetry of Extruded Mg-Zn-Ca Alloy Via Equal Channel Angular Pressing, *J. Magnes. Alloy.*, 2015, **3**(4), p 302–308. https://doi.org/10.1016/j.jma.2015.08.007

17. J.D. Robson, N. Stanford, and M.R. Barnett, Effect of Precipitate Shape and Habit on Mechanical Asymmetry in Magnesium Alloys, *Metall. Mater. Trans. A*, 2013, **44**(7), p 2984–2995. https://doi.org/10.1007/s11661-012-1466-0

18. F.W. Syed, V.A. Kumar, R.K. Gupta, and A.K. Kanjarla, Role of Microstructure on the Tension/Compression Asymmetry in a Two-Phase Ti-5Al-3Mo-1.5V Titanium Alloy, *J. Alloys Compd.*, 2019, **795**, p 151–162. https://doi.org/10.1016/j.jallcom.2019.04.272

19. Q. Zhang, J. Zhang, and Y. Wang, Effect of Strain Rate on the Tension-Compression Asymmetric Responses of Ti-6.6Al-3.3Mo-1.8Zr-0.29Si, *Mater. Des.*, 2014, **61**, p 281–285. https://doi.org/10.1016/j.matdes.2014.05.004

20. T. Neeraj, M.F. Savage, J. Tatalovich, L. Kovarik, R.W. Hayes, and M.J. Mills, Observation of Tension-Compression Asymmetry in α/β and Titanium Alloys, *Philos. Mag.*, 2005, **85**(2–3), p 279–295. https://doi.org/10.1080/14786430412331315707

21. D. Leidermark, J.J. Moverare, K. Simonsson, S. Sjostrom, and S. Johansson, Room Temperature Yield Behaviour of a Single-Crystal Nickel-Base Superalloy with Tension/Compression Asymmetry, *Comput. Mater. Sci.*, 2009, **47**(2), p 366–372. https://doi.org/10.1016/j.commatsci.2009.08.012

22. N. Tsuno, S. Shimabayashi, K. Kakehi, C.M.F. Rae, and R.C. Reed, Tension/Compression Asymmetry in Yield and Creep Strengths of Ni-based Superalloys, *Proc. Int. Symp. Superalloys*, 2008, **2008**, p 433–442

23. F. Jiao, D. Bettge, W. Osterle, and J. Ziebs, Tension-compression asymmetry of the (001) single crystal nickel base superalloy SC16 under cyclic loading at elevated temperatures, *Acta Mater.*, 1996, **44**(10), p 3933–3942. https://doi.org/10.1016/S1359-6454(96)00050-X

24. K. Zhou, B. Liu, S. Shao, and Y. Yao, Molecular dynamics simulations of tension-compression asymmetry in nanocrystalline copper, *Phys. Lett. Sect. A Gen. At. Solid State Phys.*, 2017, **381**(13), p 1163–1168. https://doi.org/10.1016/j.physleta.2017.01.027

25. M.A. Tschopp, G.J. Tucker, and D.L. McDowell, Atomistic Simulations of Tension-Compression Asymmetry in Dislocation Nucleation for Copper Grain Boundaries, *Comput. Mater. Sci.*, 2008, **44**(2), p 351–362. https://doi.org/10.1016/j.commatsci.2008.03.041

26. M.A. Tschopp and D.L. McDowell, Tension-Compression Asymmetry in Homogeneous Dislocation Nucleation in Single Crystal Copper, *Appl. Phys. Lett.*, 2007, **90**(12), p 16–18. https://doi.org/10.1063/1.2715137

27. G.G. Yapici, I.J. Beyerlein, I. Karaman, and C.N. Tome, Tension-Compression Asymmetry in Severely Deformed Pure Copper, *Acta Mater.*, 2007, **55**(14), p 4603–4613. https://doi.org/10.1016/j.actamat.2007.03.031

28. B. Yang, H. Song, S. Wang, S. Chen, and S. Zhang, Tension-Compression Mechanical Behavior and Corresponding Microstructure Evolution of Cast A356–T6 Aluminum Alloy, *Mater. Sci. Eng. A*, 2021, **821**, p 141613. https://doi.org/10.1016/j.msea.2021.141613

29. P.D. Barros, J.L. Alves, M.C. Oliveira, and L.F. Menezes, Study on the Effect of Tension-Compression Asymmetry on the Cylindrical Cup Forming of an AA2090-T3 Alloy, *Int. J. Solids Struct.*, 2018, **151**, p 135–144. https://doi.org/10.1016/j.ijsolstr.2017.06.034

30. M.T. Tucker, M.F. Horstemeyer, W.R. Whittington, K.N. Solanki, and P.M. Gullett, The Effect of Varying Strain Rates and Stress States on the plasticity, Damage, and Fracture of Aluminum Alloys, *Mech. Mater.*, 2010, **42**(10), p 895–907. https://doi.org/10.1016/j.mechmat.2010.07.003

31. S.I. Hong, Tension-Compression Asymmetry of Hardening and Damage in Al Alloy Matrix Composites, *Scr. Mater.*, 1999, **41**(4), p 433–438. https://doi.org/10.1016/S1359-6462(99)00097-4

32. L.L. Chang and L.P. Chi, Tension-Compression Asymmetry in an Extruded Mg Alloy AZ31: Texture and Strain Rate Effects, *Mater. Sci. Forum*, 2016, **849**, p 109–113. https://doi.org/10.4028/www.scientific.net/MSF.849.109

33. C. Zhang, D. Li, X. Li, and Y. Li, An Experimental Study of the Tension-Compression Asymmetry of Extruded Ti-6.5Al-2Zr-1Mo-1V Under Quasi-Static Conditions at High Temperature, *Metals (Basel)*, 2021 https://doi.org/10.3390/met11081299

34. S. Cheng, J.A. Spencer, and W.W. Milligan, Strength and Tension/Compression Asymmetry in Nanostructured and Ultrafine-Grain Metals, *Acta Mater.*, 2003, **51**(15), p 4505–4518. https://doi.org/10.1016/S1359-6454(03)00286-6

35. M. Sahoo and R.W. Smith, Mechanical Properties of Unidirectionally Solidified Al-Si Eutectic Alloys, *Met. Sci.*, 1975, **9**(1), p 217–222. https://doi.org/10.1179/030634575790444874

36. F. Vnuk, M. Sahoo, R. Van De Merwe, and R.W. Smith, The Hardness of Al-Si Eutectic Alloys, *J. Mater. Sci.*, 1979, **14**(4), p 975–982. https://doi.org/10.1007/BF00550730

37. J.M. Meininger, S.L. Dickerson, and J.C. Gibeling, Observations of Tension/Compression Asymmetry in the Cyclic Deformation of Aluminum Alloy 7075, *Fatigue Fract. Eng. Mater. Struct.*, 1996, **19**(1), p 85–97. https://doi.org/10.1111/j.1460-2695.1996.tb00934.x

38. Q. Li, S. Xue, Y. Zhang, X. Sun, H. Wang, and X. Zhang, Plastic Anisotropy and Tension-Compression Asymmetry in Nanotwinned Al-Fe Alloys: An In-Situ Micromechanical Investigation, *Int. J. Plast.*, 2020, **132**, p 102760. https://doi.org/10.1016/j.ijplas.2020.102760

39. H. Luo, L. Shaw, L.C. Zhang, and D. Miracle, On Tension/Compression Asymmetry of an Extruded Nanocrystalline Al-Fe-Cr-Ti Alloy, *Mater. Sci. Eng. A*, 2005, **409**(1–2), p 249–256. https://doi.org/10.1016/j.msea.2005.06.075

40. E. Natesan, J. Ahlstrom, S. Eriksson, and C. Persson, Effects of Temperature on the Evolution of Yield Surface and Stress Asymmetry in A356–T7 Cast Aluminium Alloy, *Materials (Basel)*, 2021, **14**(24), p 1–21. https://doi.org/10.3390/ma14247898

41. Y. Wang, J. Ding, Z. Fan, L. Tian, M. Li, H. Lu, Y. Zhang, E. Ma, J. Li, and Z. Shan, Tension-Compression Asymmetry in Amorphous Silicon, *Nat. Mater.*, 2021, **20**, p 1371–1377

42. M. Javidani and D. Larouche, Application of Cast Al-Si Alloys in Internal Combustion Engine Components, *Int. Mater. Rev.*, 2014, **59**(3), p 132–158. https://doi.org/10.1179/1743280413Y.0000000027

43. J.G. Jung, S.H. Lee, J.M. Lee, Y.H. Cho, S.H. Kim, and W.H. Yoon, Improved Mechanical Properties of Near-Eutectic Al-Si Piston Alloy through Ultrasonic Melt Treatment, *Mater. Sci. Eng. A*, 2016, **669**, p 187–195

44. A.W. Orłowicz, M. Tupaj, M. Mróz, and A. Trytek, Combustion Engine Cylinder Liners Made of Al-Si Alloys, *Arch. Foundry Eng.*, 2015, **15**(2), p 71–74. https://doi.org/10.1515/afe-2015-0041

45. F.C.R. Hernandez, J.M.H. Ramírez, and R. Mackay, Al-Si Alloys: Automotive, Aeronautical, and Aerospace Applications, Al-Si Alloy, Automotive, *Aeronaut. Aerosp. Appl.*, 2017 https://doi.org/10.1007/978-3-319-58380-8

46. Y. Kun, L. Chao, W. Richu, and Y. Jun, Production, and Properties of a Spray Formed 70%Si-Al Alloy for Electronic Packaging Applications, *Mater. Trans.*, 2008, **49**(3), p 685–687. https://doi.org/10.2320/matertrans.MRP2007630

47. Y.U. Kun, L.I. Shao-jun, C. Li-san, Z. Wei-shang, and L.I. Peng-fei, Microstructure Characterization and Thermal Properties of Hypereutectic SiíAl Alloy for Electronic Packaging Applications, *Trans. Nonferrous Met. Soc. China*, 2012, **22**(6), p 1412–1417. https://doi.org/10.1016/S1003-6326(11)61334-4

48. K. Singh and B.P. Kashyap, Effects of Remelting on Variations in Composition, Microstructure, and Hardness Property of Binary Al-Si Alloys, *J. Mater. Eng. Perform.*, 2022 https://doi.org/10.1007/s11665-022-07323-0

49. K. Kobayashi, P.H. Shingu, and R. Ozaki, Crystal Growth of the Primary Silicon in an Al-16 wt.% Si Alloy, *J. Mater. Sci.*, 1975, **10**(2), p 290–299. https://doi.org/10.1007/BF00540353

50. J.H. Hollomon, Tensile Deformation, *Trans. Metall. Soc. AIME*, 1945, **162**, p 268–290

51. E.O. Hall, The Deformation and Ageing of Mild Steel: III Discussion of Results, *Proc. Phys. Soc. Sect. B*, 1951, **64**, p 747–753

52. N.J. Petch, The Cleavage Strength of Polycrystals, *I. Iron Steel Inst.*, 1953, **174**, p 25–28

53. Z.C. Cordero, B.E. Knight, and C.A. Schuh, Six Decades of the Hall-Petch Effect—A Survey of Grain-Size Strengthening Studies on Pure Metals, *Int. Mater. Rev.*, 2016, **61**(8), p 495–512

54. A. Lasalmonie and J.L. Strudel, Influence of Grain Size on the Mechanical Behaviour of Some High Strength Materials, *J. Mater. Sci.*, 1986, **21**, p 1837–1852. https://doi.org/10.1007/BF00547918

55. N. Alshabatat and S. Al-qawabah, Effect of 4%wt. Cu Addition on the Mechanical Characteristics and Fatigue Life of Commercially Pure Aluminum, *Jordan J. Mech. Ind. Eng.*, 2015, **9**(4), p 297–301

56. G. Langelandsvik, A. Horgar, T. Furu, H.J. Roven, and O.M. Akselsen, Comparative Study of Eutectic Al-Si Alloys Manufactured by WAAM and Casting, *Int. J. Adv. Manuf. Technol.*, 2020, **110**(3–4), p 935–947. https://doi.org/10.1007/s00170-020-05735-7

57. L.J. Vandeperre, F. Giuliani, S.J. Lloyd, and W.J. Clegg, The Hardness of Silicon and Germanium, *Acta Mater.*, 2007, **55**(18), p 6307–6315. https://doi.org/10.1016/j.actamat.2007.07.036

58. T. H. Courtney, Mechanical Behavior of Materials, 2 Edition. 2009

59. M.A. Meyers and K.K. Chawla, Mechanical behavior of materials, *Choice Rev Online*, 2009 https://doi.org/10.5860/choice.46-6830

60. L. Kovarik, R.R. Unocic, J. Li, P. Sarosi, C. Shen, Y. Wang, and M.J. Mills, Microtwinning and other shearing mechanisms at intermediate temperatures in Ni-based superalloys, *Prog. Mater. Sci.*, 2009, **54**, p 839–873. https://doi.org/10.1016/j.pmatsci.2009.03.010

61. L. Zhang, R. Barrett, P. Cloetens, C. Detlefs, and M. Sanchez Del Rio, Anisotropic elasticity of silicon and its application to the modelling of x-ray optics, *J. Synchrotron Radiat.*, 2014, **21**(3), p 507–517. https://doi.org/10.1107/S1600577514004962

62. A.D. Rollett and U.F. Kocks, A review of the stages of work hardening, *Solid State Phenom.*, 1993, **35–36**, p 1–18. https://doi.org/10.4028/www.scientific.net/ssp.35-36.1

63. S.K. Shaha, F. Czerwinski, W. Kasprzak, and D.L. Chen, Work Hardening and Texture during Compression Deformation of the Al-Si-Cu-Mg Alloy Modified with V, Zr and Ti, *J. Alloys Compd.*, 2014, **593**, p 290–299. https://doi.org/10.1016/j.jallcom.2013.12.081

64. Z. Guo and W. Sha, Quantification of precipitation hardening and evolution of precipitates, *Mater. Trans.*, 2002, **43**(6), p 1273–1282. https://doi.org/10.2320/matertrans.43.1273

65. P. Taylor, M. F. Ashby, Work hardening of dispersion-hardened crystals, 2006, p 1157–1178